Cell Reports

Article

Slc12a8 in the lateral hypothalamus maintains energy metabolism and skeletal muscle functions during aging

Graphical abstract

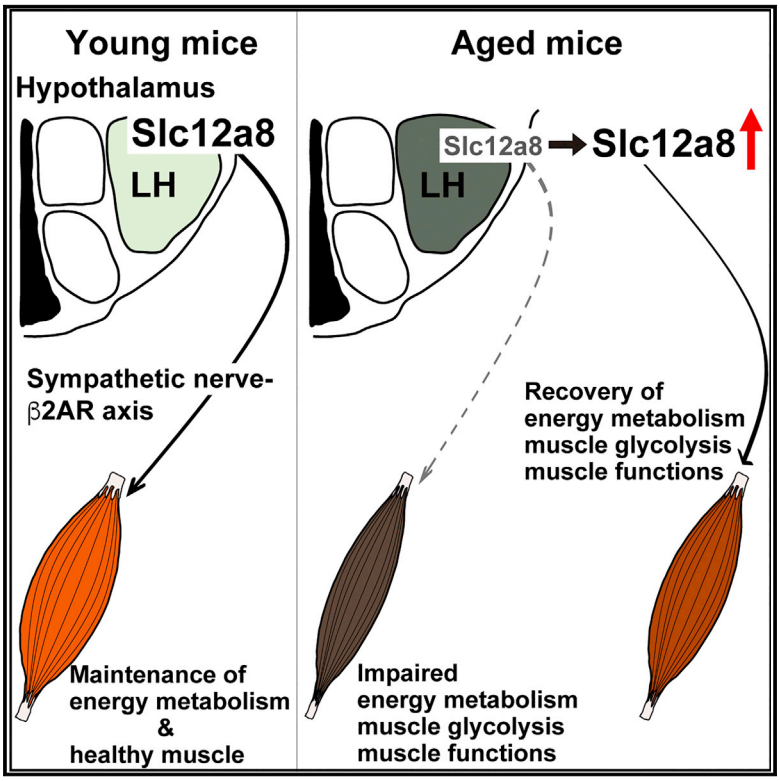

Highlights

- *Slc12a8* in the LH regulates energy expenditure and skeletal muscle functions
- The LH-skeletal muscle connection is mediated by the sympathetic nerve-β2AR axis
- LH-specific knockdown of *Slc12a8* recapitulates phenotypes in aged mice
- LH-specific overexpression of *Slc12a8* improves sarcopenia and frailty in aged mice

Authors

Naoki Ito, Ai Takatsu, Hiromi Ito, Yuka Koike, Kiyoshi Yoshioka, Yasutomi Kamei, Shin-ichiro Imai

Correspondence

imaishin@wustl.edu

In brief

Ito et al. demonstrate that *Slc12a8* in the lateral hypothalamus (LH) regulates activity-dependent energy expenditure and skeletal muscle functions through the sympathetic nerve-β2AR axis during aging. Overexpression of *Slc12a8* in the LH improves age-associated sarcopenia and frailty in mice, suggesting that *Slc12a8* could be an important target of anti-aging interventions.

Ito et al., 2022, Cell Reports *40*, 111131
July 26, 2022 © 2022 The Authors.
https://doi.org/10.1016/j.celrep.2022.111131

CellPress

Cell Reports

CellPress
OPEN ACCESS

Article

Slc12a8 in the lateral hypothalamus maintains energy metabolism and skeletal muscle functions during aging

Naoki Ito,[1,2,6] Ai Takatsu,[1,2,7] Hiromi Ito,[1,2,7] Yuka Koike,[1,2] Kiyoshi Yoshioka,[3,4] Yasutomi Kamei,[4] and Shin-ichiro Imai[1,2,5,8,*]

[1]AMED Frailty Research Laboratory (Teijin), AMED Cyclic Innovation for Clinical Empowerment (CiCLE), Osaka, Japan
[2]Laboratory of Molecular Life Science, Institute of Biomedical Research and Innovation (IBRI), Foundation for Biomedical Research and Innovation (FBRI), Kobe, Japan
[3]Institute for Research on Productive Aging (IRPA), Tokyo, Japan
[4]Laboratory of Molecular Nutrition, Graduate School of Life and Environmental Sciences, Kyoto Prefectural University, Kyoto, Japan
[5]Department of Developmental Biology, Department of Medicine, Washington University School of Medicine, St. Louis, MO, USA
[6]Present address: Brain-Skeletal Muscle Connection in Aging Project Team, Geroscience Research Center, National Center for Geriatrics and Gerontology, Obu, Japan
[7]These authors contributed equally
[8]Lead contact
*Correspondence: imaishin@wustl.edu
https://doi.org/10.1016/j.celrep.2022.111131

SUMMARY

Sarcopenia and frailty are urgent socio-economic problems worldwide. Here we demonstrate a functional connection between the lateral hypothalamus (LH) and skeletal muscle through Slc12a8, a recently identified nicotinamide mononucleotide transporter, and its relationship to sarcopenia and frailty. *Slc12a8*-expressing cells are mainly localized in the LH. LH-specific knockdown of *Slc12a8* in young mice decreases activity-dependent energy and carbohydrate expenditure and skeletal muscle functions, including muscle mass, muscle force, intramuscular glycolysis, and protein synthesis. LH-specific *Slc12a8* knockdown also decreases sympathetic nerve signals at neuromuscular junctions and β2-adrenergic receptors in skeletal muscle, indicating the importance of the LH-sympathetic nerve-β2-adrenergic receptor axis. LH-specific overexpression of *Slc12a8* in aged mice significantly ameliorates age-associated decreases in energy expenditure and skeletal muscle functions. Our results highlight an important role of *Slc12a8* in the LH for regulation of whole-body metabolism and skeletal muscle functions and provide insights into the pathogenesis of sarcopenia and frailty during aging.

INTRODUCTION

In rapidly aging societies, frailty, defined by deterioration of physical and mental functions because of aging, is an urgent socio-economical problem (Cesari et al., 2014). In particular, sarcopenia, age-related muscle weakness with decreases in muscle weight and force, is a critical pathophysiological condition that induces frailty, and development of preventive and therapeutic interventions for sarcopenia is indispensable for extension of the health-span (Kim and Choi, 2013). The underlying molecular mechanisms of sarcopenia and physical frailty still remain unclear, and, to date, few potential drug targets have been identified (Dao et al., 2020). Gaining a better understanding of the molecular mechanisms of sarcopenia and frailty will allow us to identify effective pharmacological approaches and develop therapeutic strategies to prevent and/or treat sarcopenia and frailty.

Over the past several years, some studies have revealed that progressive, systemic decreases in nicotinamide adenine dinucleotide (NAD^+) levels and the resultant dysfunctions of NAD^+-consuming enzymes are a driving force of age-associated pathophysiologies (Chini et al., 2021; Fang et al., 2014, 2019; Katsyuba et al., 2020; Rajman et al., 2018; Verdin, 2015; Yoshino et al., 2018). Supplementation of NAD^+ intermediates, such as nicotinamide riboside or nicotinamide mononucleotide (NMN), has been extensively tested to boost NAD^+ levels systemically, and their effects to counteract age-associated tissue dysfunction have been demonstrated (Chini et al., 2021; Fang et al., 2014, 2019; Katsyuba et al., 2020; Rajman et al., 2018; Verdin, 2015; Yoshino et al., 2018). It has been reported that supplementation of NMN effectively mitigates age-associated physiological decline in mice (Mills et al., 2016). Interestingly, NMN enhances energy metabolism and improves insulin sensitivity in mice. It has been demonstrated recently that NMN significantly improves skeletal muscle insulin sensitivity and signaling in humans (Yoshino et al., 2021). However, the precise mechanism for its action is still poorly investigated.

This is an open access article under the CC BY-NC-ND license (http://creativecommons.org/licenses/by-nc-nd/4.0/).

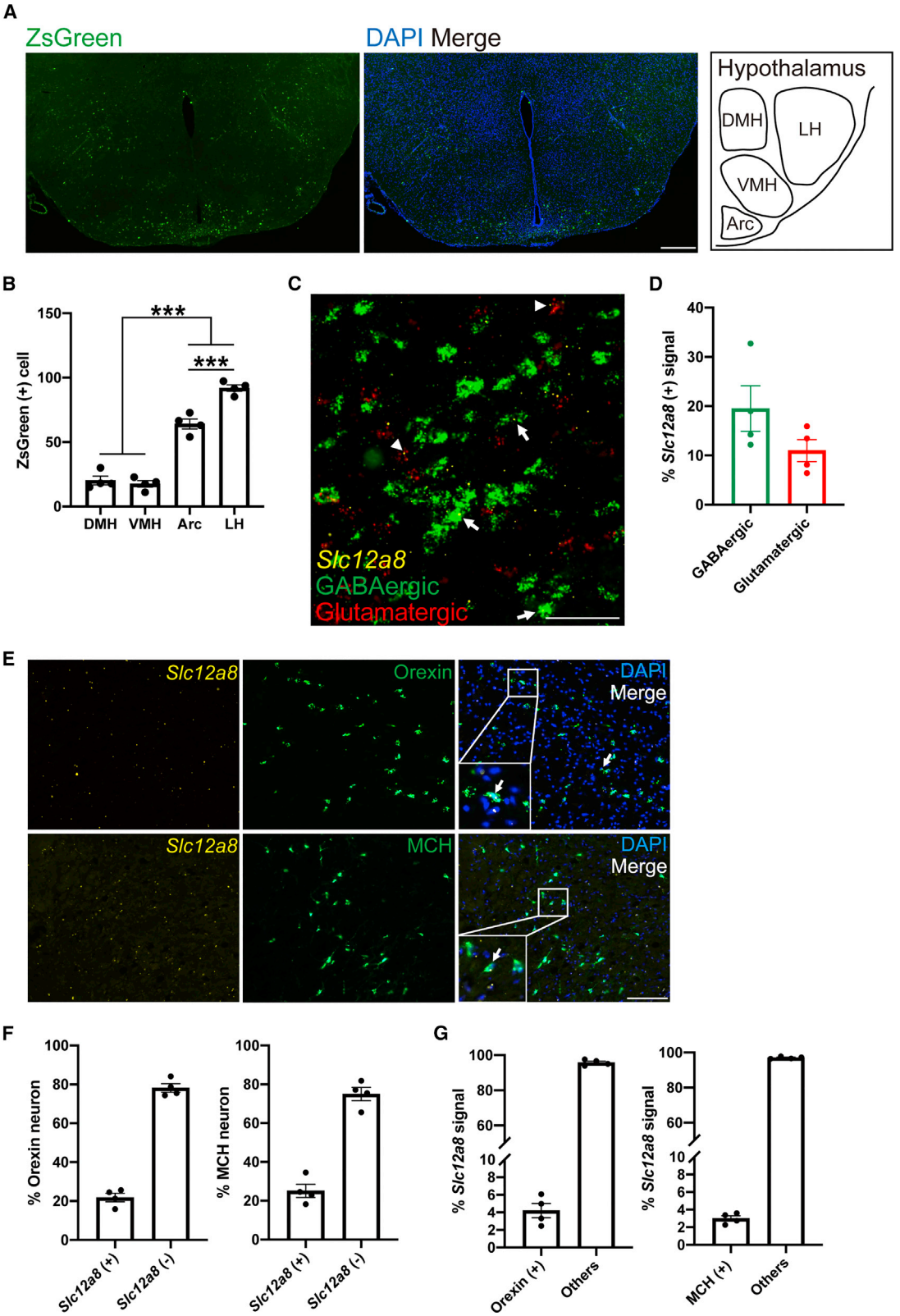

(legend on next page)

We have previously demonstrated that Sirt1, a mammalian NAD^+-dependent protein deacetylase, in the hypothalamus plays a critical role in regulation of age-associated changes in tissue functions and lifespan in mice (Satoh et al., 2013; Snyder-Warwick et al., 2018). Brain-specific *Sirt1*-overexpressing (BRASTO) mice, which show higher *Sirt1* expression in the dorsomedial hypothalamus (DMH) and lateral hypothalamus (LH), exhibit significant improvement in age-associated morphological and functional changes of mitochondria in skeletal muscle (Satoh et al., 2013). BRASTO mice maintain more youthful morphologic features of neuromuscular junctions (NMJs) compared with controls (Snyder-Warwick et al., 2018). Contrarily, knockdown of *Sirt1* in the DMH and LH in aged mice causes decreased expression of mitochondrial functional genes and β2-adrenergic receptor (*β2AR*), which is regulated by the sympathetic nerve (Khan et al., 2016), and more aged NMJ morphology in skeletal muscle (Satoh et al., 2013; Snyder-Warwick et al., 2018). These results suggest that skeletal muscle is regulated by the hypothalamic NAD^+-Sirt1 axis, potentially through the sympathetic nervous system, and that functional decline in this particular hypothalamic function may contribute to the pathogenesis of sarcopenia and frailty during the process of aging.

We have recently identified *Slc12a8* as an NMN transporter (Grozio et al., 2019). *Slc12a8* is highly expressed in the small intestine and specifically transports NMN in a sodium-dependent manner, maintaining intracellular NAD^+ levels during the process of aging. Our present study was originally initiated by our interesting finding that *Slc12a8* is also expressed in a specific neuronal subpopulation in the LH. Therefore, we suspected that *Slc12a8* in the LH might be involved in the hypothalamus-skeletal muscle interaction and that dysfunction of this interaction could be involved in the pathogenesis of sarcopenia and frailty. To address this hypothesis, we analyzed the functions of *Slc12a8* in the LH and its effects on skeletal muscle functions.

RESULTS

Slc12a8 is expressed in the LH

Because expression of *Slc12a8* in the hypothalamus is not reported, we first analyzed *Slc12a8*-expressing cells in the hypothalamus. To visualize *Slc12a8*-expressing cells, we connected the coding region of *Slc12a8* to Cre recombinase-estrogen receptor T2 (*CreERT2*) through the *P2A* sequence and generated *Slc12a8-CreERT2* knockin mice (Figure S1). We then crossed *Slc12a8-CreERT2* knockin mice with *Rosa26-CAG-LSL-ZsGreen* mice (Madisen et al., 2010). In *Slc12a8*-expressing cells, administration of tamoxifen resulted in removal of a *STOP* cassette and induced subsequent expression of ZsGreen. After 5 days of tamoxifen administration followed by 7-day recovery, we observed that the highest number of ZsGreen-positive cells was localized in the LH compared with other hypothalamic nuclei, including the arcuate nucleus (Arc), DMH, and ventromedial hypothalamus (VMH) (Figures 1A and 1B). Because we observed a relatively large number of *Slc12a8*-expressing cells in the LH, we analyzed these *Slc12a8*-expressing cells in the LH. Using RNAscope, we co-stained *Slc12a8* mRNA with *Slc32a1* mRNA, a marker of GABAergic neurons, and *Slc17a6* mRNA, a marker of glutamatergic neurons (Figure 1C). We observed that approximately 20% and 10% of the *Slc12a8* signals were positive for the GABAergic and glutamatergic neuronal markers, respectively (Figure 1D). Because orexin neurons and melanin-concentrating hormone (MCH) neurons are the most well-characterized neuronal populations in the LH (Stuber and Wise, 2016), we also co-stained *Slc12a8* mRNA with an anti-orexin antibody or anti-MCH antibody (Figure 1E). Approximately 20% of orexin neurons and MCH neurons expressed *Slc12a8* (Figures 1E and 1F, arrows). However, among *Slc12a8*-positive cells, only 3%–4% of these cells were positive for orexin or MCH (Figure 1G). These results indicate that *Slc12a8* is expressed in the LH, defining a population that is distinct from previously described neuronal populations in the LH.

Slc12a8 in the LH regulates activity-dependent energy expenditure and skeletal muscle functions

To analyze the function of *Slc12a8* in the LH, we administered a lentivirus encoding shRNA (short hairpin RNA) for *Slc12a8* (sh-*Slc12a8*) by stereotaxic injection to the LH (Figure 2A). As a control, we injected a lentivirus encoding shRNA for firefly luciferase (sh-*fLuc*). The appropriate coordinate was determined by the localization of *Slc12a8*-positive cells. The knockdown efficiency of *Slc12a8* shRNA was approximately 40% (Figure 2B). Similar to previous results (Grozio et al., 2019), knockdown of *Slc12a8* in Neuro2a cells resulted in an impaired NMN-induced increase in NAD^+ levels (Figures S2A and S2B). We first evaluated the energy expenditure of LH-specific *Slc12a8* knockdown (KD) mice using metabolic cages with running wheels (Chen et al., 2020; Okamoto et al., 2018). Three months after injection of the

Figure 1. *Slc12a8*-expressing cells are localized in the LH

(A) Representative immunofluorescence image of ZsGreen in tamoxifen-treated *Slc12a8-CreERT2*/*Rosa26-ZsGreen* mice. Schematics of major hypothalamic nuclei, including the dorsomedial hypothalamus (DMH), ventromedial hypothalamus (VMH), arcuate nucleus (Arc), and lateral hypothalamus (LH), is shown on the right. Coordinates were as follows: relative to the bregma; anterior-posterior, −1.8 mm; medial-lateral, ±0.9 mm; dorsal-ventral, −5.4 mm. Scale bar, 300 μm.

(B) Quantitative analysis of ZsGreen-positive cells in each hypothalamic nucleus. n = 4.

(C) Representative image for *Slc12a8* mRNA (yellow), *Slc32a1* mRNA (a marker for GABAergic neurons, green), and *Slc17a6* mRNA (a marker for glutamatergic neurons, red) in the LH by RNAscope. Arrows and arrowheads indicate *Slc12a8*-positive GABAergic neurons and *Slc12a8*-positive glutamatergic neurons, respectively. Scale bar, 50 μm.

(D) Quantitative analysis of *Slc12a8*-positive GABAergic neurons and glutamatergic neurons. n = 4.

(E) Representative image of *Slc12a8* mRNA (yellow) and orexin (green, top), or *Slc12a8* mRNA and MCH (green, bottom). Arrows indicate *Slc12a8*-positive orexin neurons or an MCH neuron. Scale bar, 100 μm.

(F) Quantitative analysis of *Slc12a8*-positive and -negative orexin neurons (left) or MCH neurons (right). n = 4.

(G) Quantitative analysis of orexin-positive (left) or MCH-positive (right) *Slc12a8* mRNA signals. n = 4.

All images were captured in the LH of 3- to 4-month-old mice. ***$p < 0.001$ by one-way ANOVA with Tukey's test for (B). Error bars indicate SEM.

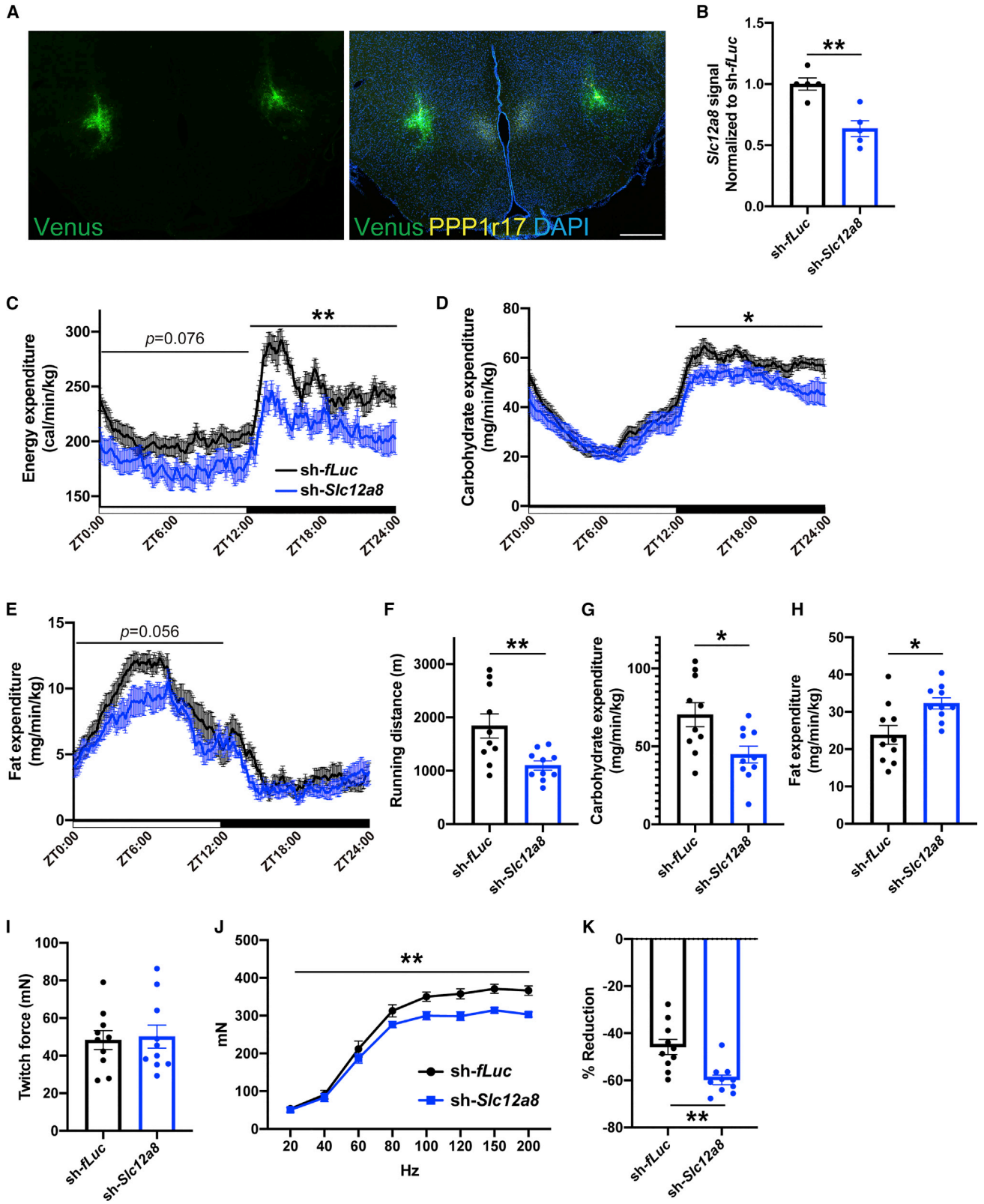

(legend on next page)

lentivirus, *Slc12a8* KD mice showed significantly decreased energy expenditure during the dark time (Figures 2C and S2C, left panel). We also observed a tendency for a decrease in energy expenditure during the light time. We also analyzed which energy source was the major cause of the decreased energy expenditure in *Slc12a8* KD mice. *Slc12a8* KD mice displayed significant decreases in carbohydrate expenditure during the dark time (Figures 2D and S2D, left panel). On the other hand, we observed mild decreases in fat expenditure only during the light time (Figures 2E and S2E, left panel). When we removed the wheels, we did not observe any changes in energy expenditure or carbohydrate expenditure in *Slc12a8* KD mice (Figures S2C–S2E, right panels), indicating that these decreases in energy expenditure and carbohydrate expenditure in *Slc12a8* KD mice are activity dependent. There were no significant differences in respiratory exchange ratio (RER) between *Slc12a8* KD mice and control mice (Figures S2F and S2G). Because *Slc12a8* KD mice showed no differences in food intake (Figure S2H), daily open-field activity in a cage (Figure S2I), or voluntary wheel running distance (Figure S2J), the decreases in energy and carbohydrate expenditure are not due to decreased food intake or daily activity. We also performed a long-term (1 month) voluntary running exercise experiment and analyzed the expression of *Slc12a8*. However, there were no changes in expression of *Slc12a8* in the hypothalamus (data not shown). The rectal temperature in *Slc12a8* KD mice was comparable with that in control mice (Figure S2K). Thus, *Slc12a8* in the LH regulates activity-dependent energy expenditure and carbohydrate expenditure.

Given that *Slc12a8* deficiency causes decreases in NAD^+ levels *in vivo* (Grozio et al., 2019), we expected to see NAD^+ decreases in the LH. However, it was technically difficult to reliably measure NAD^+ levels specifically in such a small *Slc12a8*-positive area of the LH. Thus, we decided to knock down nicotinamide phosphoribosyl transferase (*Nampt*), the rate-limiting enzyme for the major NAD^+ biosynthetic pathway, in the LH. Similar to *Slc12a8* KD mice, LH-specific *Nampt* KD mice also showed significant decreases in energy and carbohydrate expenditure (Figures S2N–S2P), suggesting that decreased NAD^+ levels were most likely the cause of the phenotypes in *Slc12a8* KD mice.

Because decreases in energy expenditure and carbohydrate expenditure in *Slc12a8* KD mice were observed only during the dark time and were activity dependent (Figures 2C, 2D, S2C, and S2D), we hypothesized that these decreases in energy and carbohydrate expenditure could be caused by defects in skeletal muscle functions. We first performed a treadmill test. *Slc12a8* KD mice exhibited approximately 40% decreases in running distance, indicating that *Slc12a8* in the LH regulates endurance capacity (Figure 2F). Although oxygen consumption and energy expenditure at the maximum speed were equivalent in control and *Slc12a8* KD mice (Figure S2L; data not shown), *Slc12a8* KD mice showed decreased carbohydrate expenditure at the maximum speed (Figure 2G) and increased fat expenditure and decreased RER (Figures 2H and S2M). These results indicate that *Slc12a8* KD mice have defects in activity-dependent utilization of carbohydrates and that this impairment of carbohydrate expenditure may cause decreased endurance capacity. We next measured skeletal muscle force *in vivo* (Myers et al., 2019). There was no difference in the twitch force induced by single electrical stimulation between control and *Slc12a8* KD mice (Figure 2I). However, *Slc12a8* KD mice showed clear decreases in muscle force during high-frequency electrical stimulation (Figure 2J), indicating that maximum strength is impaired in *Slc12a8* KD mice. We also evaluated fatigue resistance by repeatedly stimulating skeletal muscle. Control mice showed approximately 40% decreases in muscle force during repeated stimulation, whereas *Slc12a8* KD mice showed approximately 60% decreases, suggesting that *Slc12a8* KD mice are more susceptible to fatigue compared with control mice (Figure 2K). These findings indicate that *Slc12a8* in the LH is required for maintenance of endurance capacity, muscle force, and fatigue resistance.

Slc12a8 in the LH regulates skeletal muscle mass through protein synthesis

Because observed decreases in carbohydrate expenditure (Figures 2D and 2G), maximum strength (Figure 2J), and fatigue resistance (Figure 2K) implicated defects in fast muscle fibers (Talbot and Maves, 2016), we hypothesized that *Slc12a8* in the LH mainly controlled fast muscles. Fast muscles rely on glycolytic metabolism as their energy source. Therefore, we analyzed the tissue weights of the hindlimb muscles including fast and slow muscles. Consistent with our hypothesis, we detected significant decreases in tissue weights of fast muscles, including the tibialis anterior (TA), gastrocnemius (GAS), plantaris (PLA), and quadriceps (QUA) muscles, but not in the soleus (SOL) muscle, in *Slc12a8* KD mice (Figure 3A). The extensor digitorum longus (EDL) muscle also showed a tendency of decrease in muscle weight. We did not observe differences in heart and epididymal fat weights (Figure S3A). Body weight changes after stereotaxic injection of the lentivirus were equivalent in control and *Slc12a8* KD mice (Figure S3B). We also analyzed changes in cross-sectional area of muscle fibers in control and *Slc12a8* KD mice. We performed immunostaining of type 1, type 2A, and type 2B muscle fibers using the GAS muscle. Although the

Figure 2. *Slc12a8* in the LH regulates energy expenditure and skeletal muscle functions

(A) Representative images of the immunohistochemistry of Venus derived from a lentivirus. Ppp1r17 was stained for a marker of the DMH compact region (Caglar and Friedman, 2021). Scale bar, 300 μm.

(B) Quantitative analysis of the KD efficiency of *Slc12a8* by RNAscope. n = 4–5.

(C–E) Metabolic cage analysis for energy expenditure (C), carbohydrate expenditure (D), and fat expenditure (E) of LH-specific *Slc12a8* KD mice. n = 8.

(F) Endurance capacity of LH-specific *Slc12a8* KD mice by treadmill analysis. n = 10.

(G and H) Carbohydrate expenditure (G) and fat expenditure (H) at maximum speed of LH-specific *Slc12a8* KD mice. n = 10.

(I) Twitch force measurement of LH-specific *Slc12a8* KD mice. n = 10.

(J) *In vivo* muscle force-frequency curve of LH-specific *Slc12a8* KD mice. n = 10.

(K) Force reduction during repeated electrical stimulation in LH-specific *Slc12a8* KD mice. n = 10.

*$p < 0.05$ and **$p < 0.01$ by Student's t test for (B), (F)–(I), and (K) or by two-way repeated-measures ANOVA for (C)–(E) and (J). Error bars indicate SEM.

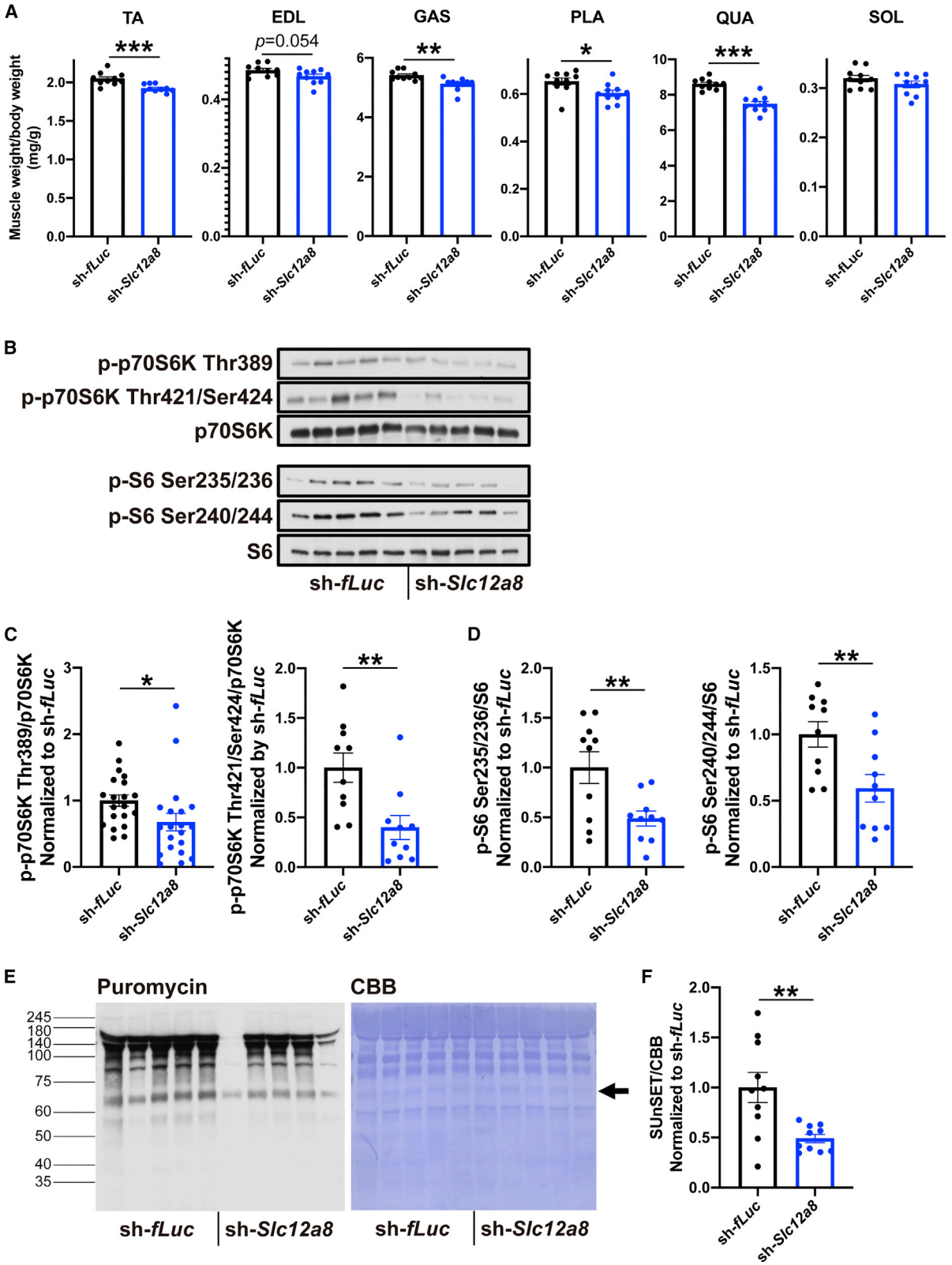

(legend on next page)

cross-sectional areas of type 1 fibers in *Slc12a8* KD mice were comparable with those in control mice (Figures S3C and S3D), the cross-sectional areas of type 2A and type 2B fibers in *Slc12a8* KD mice were significantly smaller than those in control mice (Figures S3C, S3E, and S3F). These results strongly suggest that *Slc12a8* in the LH is required for maintenance of fast muscle fibers.

Because the balance of protein synthesis and protein degradation determines skeletal muscle mass (Egerman and Glass, 2014), we analyzed signaling molecules that regulate protein synthesis and degradation. We found that phosphorylation of p70S6K, a central molecule that regulates protein synthesis, was decreased in the TA muscles of *Slc12a8* KD mice (Figures 3B and 3C). Phosphorylation of S6, a downstream target of p70S6K, was also decreased in *Slc12a8* KD mice (Figures 3B and 3D), indicating that the signaling cascade controlling protein synthesis is downregulated in *Slc12a8* KD mice. To measure changes in protein synthesis, we administered puromycin and detected newly synthesized puromycin-labeled peptides, a method called surface sensing of translation (SUnSET) analysis (Goodman and Hornberger, 2013). We found that the amounts of puromycin-labeled peptides were decreased in *Slc12a8* KD mice (Figures 3E and 3F), indicating that *Slc12a8* in the LH maintains fast muscle weight by regulating protein synthesis. It is well known that Akt acts as an upstream kinase for protein synthesis and degradation (Egerman and Glass, 2014). Thus, we analyzed phosphorylation levels of Akt in TA muscles of control and *Slc12a8* KD mice. As opposed to p70S6K and S6, phosphorylation of Akt at Thr308 was increased in *Slc12a8* KD mice (Figures S3G and S3H). There were no differences in phosphorylation of Akt at Ser473. It is possible that Akt phosphorylation increases in response to the decrease in phosphorylation of p70S6K and S6 (Bentzinger et al., 2008). We also analyzed phosphorylation of FoxOs, the central molecules for protein degradation that act downstream of Akt. We observed no differences in phosphorylation levels of FoxO1 and FoxO3a and expression of their targets, MuRF-1 and atrogin-1, between control and *Slc12a8* KD mice (data not shown). Our findings indicate that *Slc12a8* in the LH regulates skeletal muscle mass through protein synthesis.

Slc12a8 in the LH regulates glycolysis by regulating the sympathetic nerve-β2-adrenergic receptor (β2AR) axis in skeletal muscle

Because *Slc12a8* KD mice showed decreased carbohydrate expenditure (Figures 2D and 2G), we focused on glucose metabolism in skeletal muscle. We first analyzed the main glycolysis-related metabolites. The amounts of glycogen and glucose in the TA muscle of *Slc12a8* KD mice were comparable with those of control mice (Figures 4A and 4B). However, we found that the amounts of pyruvate, an end product of glycolysis, were significantly decreased to approximately 40% in *Slc12a8* KD mice (Figure 4C), suggesting decreased glycolysis in *Slc12a8* KD mice. At a systemic level, we did not observe any abnormalities in fed and fasted blood glucose levels, glucose tolerance tests (GTTs), and insulin tolerance tests (ITTs) in *Slc12a8* KD mice (Figures S4A–S4C), implying that defects in glucose metabolism might be limited only in skeletal muscle. Thus, we analyzed glycolysis-related gene expression in skeletal muscle and found that the expression levels of peroxisome proliferator-activated receptor delta (*PPARδ*), *PPARγ*, and pyruvate dehydrogenase kinase 4 (*PDK4*) were significantly decreased in *Slc12a8* KD mice (Figure 4D). There was no difference in expression of *PPARα*. *PPARδ* and *PPARγ* are essential regulators of glucose metabolism in skeletal muscle (Grygiel-Gorniak, 2014; Hong et al., 2019). Activation of *PPARδ* in skeletal muscle results in increased glucose utilization *in vitro* and *in vivo* (Gan et al., 2011; Kramer et al., 2005). Overexpression of *PPARγ* in skeletal muscle causes increased glucose uptake (Amin et al., 2010). PDK4 phosphorylates pyruvate dehydrogenase (PDH) to inhibit utilization of pyruvate formed from glycolysis, controlling the balance of glucose and fatty acid utilization (Atas et al., 2020). *PDK2/PDK4* double-knockout mice show decreased phosphorylation of PDH, impaired insulin-induced glucose uptake, and decreased basal levels of glucose-6-phosphate content, an intermediary metabolite of glycolysis, in skeletal muscle (Rahimi et al., 2014). Consistent with the decreased expression of *PDK4*, phosphorylation of PDH was decreased in *Slc12a8* KD mice (Figure 4E). We also confirmed that intracellular pyruvate levels were decreased by knocking down *PDK4 in vitro* in myotubes (Figures S4D and S4E). These results suggest that *Slc12a8* in the LH regulates glycolysis in skeletal muscle by regulating *PPARδ*, *PPARγ*, and *PDK4*. Because KD of *PDK4* caused decreased phosphorylation of p70S6K and S6 (Figures S4F and S4G), the decreased protein synthesis in *Slc12a8*-KD mice is most likely induced by decreased expression of *PDK4*.

Recent studies have demonstrated that skeletal muscle is innervated by the sympathetic nerve, and stimulation of sympathetic nerves activates skeletal muscle function through β2AR (Khan et al., 2016; Straka et al., 2018). Thus, we analyzed the sympathetic nerve-β2AR axis. Similar to an earlier report (Khan et al., 2016), we confirmed that β2AR was highly expressed in NMJs (Figure S4H) and that formoterol, a long-acting β2 agonist, increased expression of *PDK4*, *PPARδ*, and *PPARγ* in skeletal muscle *in vivo* (Figure S4I) (Chinsomboon et al., 2009; Pearen et al., 2008). We found that protein expression of β2AR was significantly decreased by 80% in *Slc12a8* KD mice (Figure 4F). We also analyzed innervation of the sympathetic nerve by staining with tyrosine hydroxylase (TH), a marker of the sympathetic nerve, at NMJs (Khan et al., 2016). TH-positive signal levels

Figure 3. *Slc12a8* in the LH regulates muscle mass through protein synthesis

(A) Hindlimb muscle weights of LH-specific *Slc12a8* KD mice. n = 10.

(B) Representative western blotting for phosphorylated and total p70S6K (top) and S6 (bottom) of TA muscles from LH-specific *Slc12a8* KD mice.

(C and D) Quantitative analysis of the phosphorylation levels of p70S6K (C) and S6 (D) in LH-specific *Slc12a8* KD mice. n = 10–20.

(E) Representative images of puromycin labeled-peptides (left) and CBB (Coomassie Brilliant Blue) staining (right) of LH-specific *Slc12a8* KD mice.

(F) Quantitative analysis of (E).

Signals around 65 kDa (arrow in E) were quantified. n = 10. *$p < 0.05$, **$p < 0.01$, and ***$p < 0.001$ by Student's t test. Error bars indicate SEM.

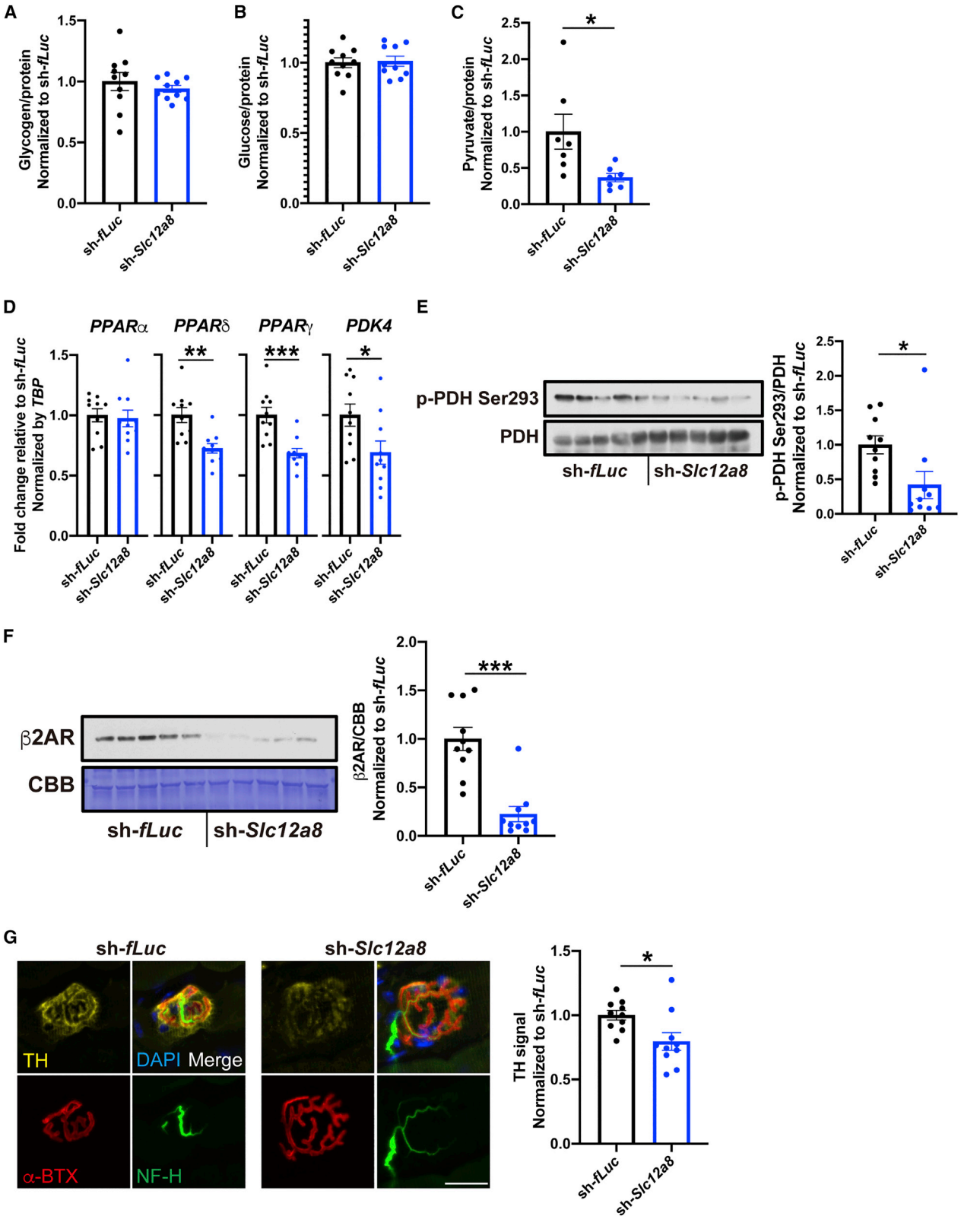

(legend on next page)

around NMJs were suppressed in *Slc12a8* KD mice (Figure 4G), suggesting that regulation of glucose metabolism by the sympathetic nerve-β2AR axis is affected in skeletal muscle of *Slc12a8* KD mice.

Slc12a8-KD mice recapitulate phenotypes in aged mice

It has been reported that aged mice show significant decreases in skeletal muscle mass and maximum strength (Ham et al., 2020). Thus, we became interested in whether *Slc12a8*-KD mice could recapitulate molecular phenotypes of aged mice. During the process of aging, expression of *Slc12a8* in the LH decreased in 18- to 20-month-old mice compared with 3- to 4-month-old mice at an extent similar to KD efficiency (Figure 5A). Protein expression of β2AR in skeletal muscle was also dramatically decreased during aging, consistent with that in *Slc12a8* KD mice (Figure 5B). Expression of *PDK4* and the amounts of pyruvate in skeletal muscle were also gradually decreased during aging, whereas expression of *PPAR*s was not altered (Figures 5C and 5D). Therefore, *Slc12a8* KD mice recapitulated molecular phenotypes observed in aged mice, suggesting involvement of *Slc12a8* in the LH for the pathogenesis of age-associated sarcopenia and frailty.

Overexpression of *Slc12a8* in the LH of aged mice improves age-related dysfunction of energy expenditure and skeletal muscle functions

Because LH-specific KD of *Slc12a8* recapitulates aging phenotypes, we expected that increasing *Slc12a8* expression in the aged LH could improve reduced energy expenditure and skeletal muscle functions in aged mice. We overexpressed *Slc12a8* in the LH of aged mice by stereotaxic injection of a lentivirus encoding *Slc12a8* (OE-*Slc12a8*). LH-specific *Slc12a8* signals detected by RNAscope were doubled by overexpression of *Slc12a8* (Figure S5A). Three months after lentivirus injection, we found that overexpression of *Slc12a8* in the LH resulted in increased energy and carbohydrate expenditure in aged mice during light and dark times (Figures 6A, 6B, S5B, and S5C). Fat expenditure was increased only during the light time in aged, LH-specific *Slc12a8*-overexpressing (*Slc12a8*-OE) mice (Figures 6C and S5D). There was no difference in RER between aged *Slc12a8*-OE mice and control mice (Figures S5E and S5F). Although we did not observe any changes in food intake, daily activity in the cage, or voluntary wheel running distance (Figures S5G–S5I), aged *Slc12a8*-OE mice showed approximately 0.6°C increases in rectal temperature (Figure 6D). Thus, overexpression of *Slc12a8* in the LH significantly ameliorated age-related dysfunction of whole-body metabolism. We next analyzed endurance capacity by a treadmill test. Aged *Slc12a8*-OE mice showed approximately 70% increases in running distance with increased carbohydrate expenditure at maximum speed (Figures 6E and 6F). There was no difference in fat expenditure (Figure 6G). RER at maximum speed tended to increase in aged *Slc12a8*-OE mice (Figure S5J). These results indicate that overexpression of *Slc12a8* in the LH enhances endurance capacity, accompanied by enhanced carbohydrate expenditure. We also analyzed muscle force *in vivo*. There was no difference in twitch force between aged *Slc12a8*-OE mice and control mice (Figure 6H). However, compared with control mice, aged *Slc12a8*-OE mice showed enhanced muscle force during high-frequency electrical stimulation (Figure 6I), demonstrating that age-associated dysfunction in maximum strength is ameliorated by overexpression of *Slc12a8* in the LH. Fatigue resistance in aged *Slc12a8*-OE mice was not altered (Figure 6J). Thus, increasing the *Slc12a8* dosage in the LH can restore younger functions of skeletal muscle in aged mice.

Finally, we evaluated tissue and molecular restoration in aged *Slc12a8*-OE mice. Aged *Slc12a8*-OE mice showed increased TA, GAS, and QUA muscle weights compared with control mice (Figure 7A). Although the cross-sectional areas of type 1 fibers in aged *Slc12a8*-OE mice were comparable with those in control mice (Figure S6A and S6B), the cross-sectional areas of type 2A and type 2B fibers in aged *Slc12a8*-OE mice were significantly larger than those in control mice (Figures S6A, S6C, and S6D). Remarkably, the expression of β2AR was increased in aged *Slc12a8*-OE mice (Figure 7B). Expression of *PDK4* and the amounts of pyruvate, which were decreased in *Slc12a8* KD mice and aged mice (Figures 4 and 5), were significantly increased in aged *Slc12a8*-OE mice (Figures 7C and 7D). The intensity of TH-positive signals around NMJs was enhanced in aged *Slc12a8*-OE mice (Figure 7E), indicating that age-associated dysregulation of the skeletal muscle-directed sympathetic nervous system was ameliorated by overexpression of *Slc12a8* in the LH of aged mice. These findings demonstrate that Slc12a8 in the LH plays a critical role in regulating energy expenditure and skeletal muscle functions and that overexpression of *Slc12a8* in the LH can ameliorate the age-associated impairments in energy metabolism and skeletal muscle functions in aged mice (Figure 7F).

DISCUSSION

In this study, we demonstrated that (1) *Slc12a8* is expressed in the LH; (2) KD of *Slc12a8* in the LH of young mice reduces activity-dependent energy expenditure and skeletal muscle functions, decreases skeletal muscle mass through impaired protein synthesis, and causes a decrease in glycolysis

Figure 4. *Slc12a8* in the LH regulates glycolysis through the sympathetic nerve-β2AR axis

(A–C) Amounts of glycogen (A), glucose (B), and pyruvate (C) in LH-specific *Slc12a8* KD mice. n = 7–10.

(D) mRNA expression levels of *PPARα*, *PPARδ*, *PPARγ*, and *PDK4* in LH-specific *Slc12a8* KD mice. n = 10.

(E) Representative western blotting for phosphorylated and total PDH (left) and quantitative analysis of the phosphorylation of PDH (right). n = 10.

(F) Representative western blotting for β2AR (left) and its quantitative analysis in LH-specific *Slc12a8* KD mice (right). n = 10.

(G) Representative images of TH (a marker of the sympathetic nerve, yellow), α-BTX (a marker of NMJs, red), and neurofilament-H (NF-H; a marker of motor neurons, green) in LH-specific *Slc12a8* KD mice (left) and quantitative analysis of TH signals around NMJs in LH-specific *Slc12a8* KD mice (right). n = 10.

*p < 0.05 and ***p < 0.001 by Student's t test. Error bars indicate SEM.

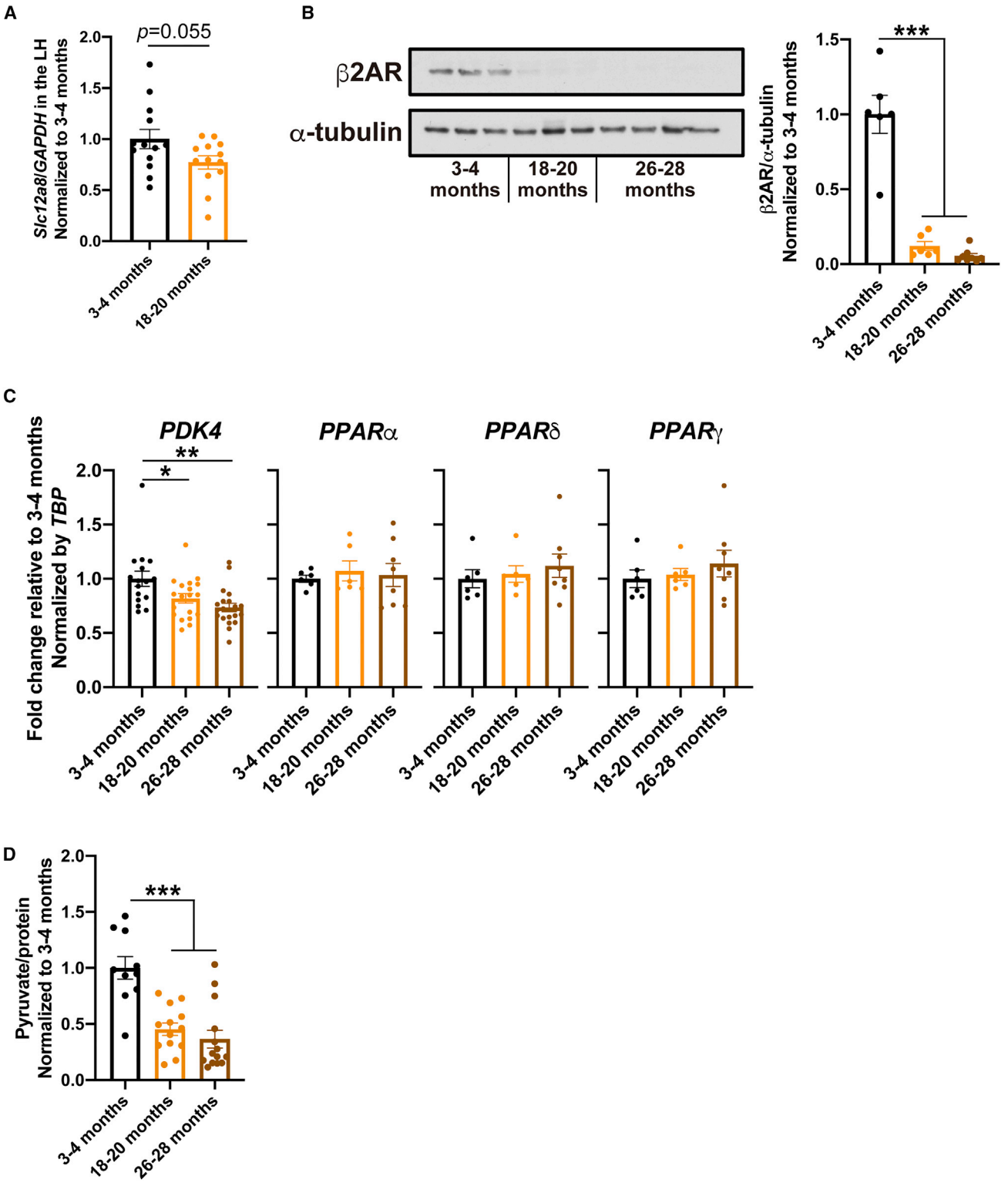

(legend on next page)

through an impaired sympathetic nerve-β2AR axis; (3) *Slc12a8*-KD mice recapitulate molecular phenotypes in aged mice; and (4) overexpression of *Slc12a8* in the LH of aged mice ameliorates the age-associated dysfunctions of energy expenditure and skeletal muscle functions. These findings strongly suggest importance of *Slc12a8* in the LH in the pathogenesis of age-associated sarcopenia and frailty. Although hypothalamic regulation of skeletal muscle function still remains underinvestigated, much work has been directed toward regulation of glucose metabolism. For instance, it has been reported that glucose uptake in skeletal muscle is induced by injection of orexin-A into the VMH (Shiuchi et al., 2009). Orexin receptors in the ventral median raphe nucleus and raphe pallidus serotonergic neurons regulate glucose utilization in brown adipose tissue and skeletal muscle (Xiao et al., 2021). We have shown previously that overexpression of *Sirt1* in the DMH and LH improves age-associated morphological changes of mitochondria and NMJs in skeletal muscle (Satoh et al., 2013; Snyder-Warwick et al., 2018) and that loss of function of *Sirt1* in the DMH and LH causes decreased expression of mitochondrial functional genes and *β2AR* in skeletal muscle, indicating the importance of the hypothalamic NAD^+-Sirt1 axis in regulation of skeletal muscle function. Our present study is able to add another key component to this axis, Slc12a8, and reveals the physiological relevance of the *Slc12a8* NMN transporter in regulation of activity-dependent energy expenditure and skeletal muscle functions during the process of aging.

Our findings demonstrate that the connection between the LH and skeletal muscle is mediated by the sympathetic nerve-β2AR axis. The major role of sympathetic innervation in skeletal muscle has long been considered for vasoconstriction. Recently, direct innervation of sympathetic nerves to skeletal muscle NMJs has been reported (Khan et al., 2016; Straka et al., 2018). Although the role of sympathetic innervation in regulation of skeletal muscle function is still under extensive investigation, it has been reported that the abundance, distribution, and maintenance of acetylcholine receptors and muscle mass are regulated by sympathetic nerves in skeletal muscle (Khan et al., 2016; Rodrigues et al., 2019; Snyder-Warwick et al., 2018). We have shown previously that KD of *Sirt1* in the DMH and LH causes decreased sympathetic regulation in skeletal muscle (Satoh et al., 2013; Snyder-Warwick et al., 2018). We showed in the present study that KD of *Slc12a8* in the LH causes significant decreases in β2AR and TH signals at NMJs and induces sarcopenic and frailty-like phenotypes in mice (Figure 4G), suggesting that the LH is involved in sympathetic regulation of skeletal muscle function.

Our findings showed that *Slc12a8* in the LH is one of the essential regulators of β2AR in skeletal muscle. The functional roles of β2AR in skeletal muscle are well studied (Santulli and Iaccarino, 2013). Administration of its agonists, such as formoterol or clenbuterol, induces muscle hypertrophy, protein synthesis, and metabolism-related gene expression. Expression of β2AR in skeletal muscle was dramatically decreased during aging (Figure 5B), suggesting that loss of β2AR signaling contributes to age-associated dysfunction of skeletal muscle. It has been reported that administration of β2AR agonists is beneficial for age-associated functional and molecular dysfunction of skeletal muscle (Conte et al., 2012; Ryall et al., 2004; Schertzer et al., 2005). Because the phenotypes of LH-specific *Slc12a8* KD or aged *Slc12a8*-OE mice are consistent with the previously reported functions of β2AR (Conte et al., 2012; Ryall et al., 2004; Santulli and Iaccarino, 2013; Schertzer et al., 2005), the link between *Slc12a8* in the LH and skeletal muscle is most likely mediated by β2AR.

We also showed that phosphorylation levels of p70S6K/S6 and protein synthesis are decreased in *Slc12a8* KD mice (Figure 3). KD of *PDK4 in vitro* in myotubes showed decreased phosphorylation of p70S6K/S6 (Figure S4F and S4G), suggesting that *PDK4* acts as a hub molecule for regulation of glycolysis and protein synthesis and that metabolic changes precede changes in protein synthesis. Decreased phosphorylation of p70S6K by KD of *PDK4* is also observed in NIH 3T3 cells (Liu et al., 2014). The phosphorylation levels of Akt, an upstream kinase of p70S6K/S6, were not decreased in *Slc12a8* KD mice or *PDK4* KD myotube (Figures S3G, S3H, S4F, and S4G), suggesting that the decreased phosphorylation of p70S6K/S6 is independent of Akt. This inverse correlation for phosphorylation of Akt and p70S6K/S6 also suggests that the phenotype of *Slc12a8* KD mice is not due to a decreased growth hormone (GH)/insulin growth factor 1 (IGF-1) axis because GH and IGF-1 can induce activation of the Akt-p70S6K-S6 axis (Egerman and Glass, 2014). One possible explanation for this inverse correlation is the negative feedback in this pathway (Yoon, 2017). Muscle-specific knockout of raptor, a regulator of mammalian target of rapamycin that acts as an upstream regulator of p70S6K/S6, shows decreased phosphorylation of p70S6K/S6, whereas phosphorylation levels of Akt are increased (Bentzinger et al., 2008). Because Akt is regulated by growth factors that are important for muscle development and growth (Egerman and Glass, 2014), the LH might regulate protein synthesis and muscle mass independent of growth factors through the sympathetic nerve-β2AR axis. The molecular mechanism by which *PDK4* regulates protein synthesis in skeletal muscle will need to be examined.

Given that skeletal muscle is one of the major tissues for amino acid metabolism (Wagenmakers, 1998), responding to systemic

Figure 5. LH-specific *Slc12a8*-KD mice recapitulate phenotypes in aged mice

(A) Expression of *Slc12a8* in the LH in 3- to 4-month-old and 18- to 20-month-old mice. n = 13.

(B) Left: representative images of western blotting for β2AR in 3- to 4-month-old, 18- to 20-month-old, and 26- to 28-month-old mice. Right: quantitative analysis of the time course changes of β2AR expression. n = 6–8.

(C) Time course changes for the expression of *PDK4*, *PPARα*, *PPARδ*, and *PPARγ* in skeletal muscle. n = 6–20.

(D) Time course changes for the amounts of pyruvate in skeletal muscle. n = 10–14.

*p < 0.05, **p < 0.01, and ***p < 0.001 by Student's t test for (A) or one-way ANOVA with Tukey's test for (B)–(D). Error bars indicate SEM.

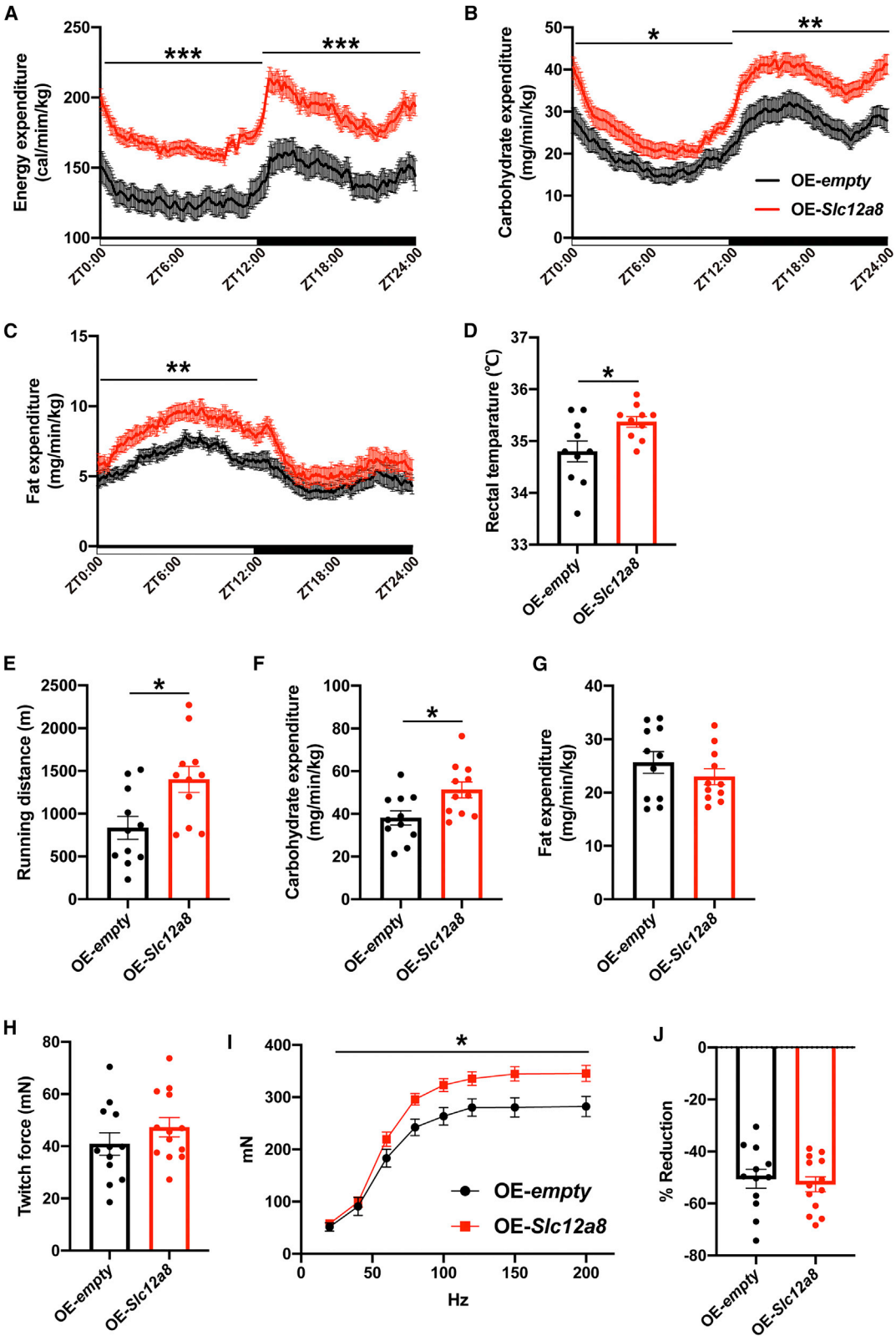

(legend on next page)

amino acid and/or glucose deficiency by inducing protein degradation under nutritional depletion (Shimizu et al., 2015), *Slc12a8* in the LH may control the balance between two different aspects of skeletal muscle function: a metabolic tissue that needs to maintain amino acids and a mechanical tissue that needs to maintain locomotive activity. It will be of great interest to examine whether *Slc12a8* in the LH is critical for skeletal muscle to respond to nutritional changes, such as caloric restriction and a high-fat diet.

Regulation of feeding behavior by the LH has been well studied, and the food intake of *Slc12a8* KD mice was comparable with that of control mice (Figure S2H). Incomplete KD efficiency of *Slc12a8* could be an explanation. Another possibility is that *Slc12a8*-expressing cells comprise different cell populations that are not involved in feeding behavior. Only 3%–4% of *Slc12a8*-expressing cells were positive for orexin or MCH (Figures 1E and 1G). Further characterization of *Slc12a8*-expressing cells in the LH will shed lights onto how exactly the LH regulates skeletal muscle and contributes to the pathogenesis of sarcopenia and frailty.

We also found that *Slc12a8* in the LH regulates activity-dependent energy and carbohydrate expenditure. However, expression of *Slc12a8* in the hypothalamus was not affected by 1-month-long voluntary exercise, suggesting that beneficial effects of exercise on skeletal muscle are not due to increased expression of *Slc12a8* in the hypothalamus.

Remarkably, overexpression of *Slc12a8* in the LH was able to ameliorate age-associated decreases in energy metabolism and skeletal muscle functions in aged mice (Figures 6 and 7). Although the underlying molecular mechanisms of sarcopenia and frailty are multifaceted and still controversial (Kim and Choi, 2013), abnormalities in neural functions have been speculated to be one of the causes of sarcopenia and frailty. Our results clearly showed that a reduction in *Slc12a8* expression in the LH, at least in part, causes age-associated sarcopenic and frailty-like phenotypes in mice. In this regard, a more precise analysis will be necessary for the time course of changes in *Slc12a8* expression in the LH and skeletal muscle force and metabolism. We were able to ameliorate these age-associated functional decreases in energy metabolism and skeletal muscle functions by enhancing the function of *Slc12a8* in the LH in aged mice. It will be of great importance to directly manipulate the activity of *Slc12a8*-positive neurons by designer receptors exclusively activated by designer drugs (DREADDs) and examine whether sarcopenic and frailty phenotypes can be ameliorated in aged mice. A more translatable approach would be to find compounds that could activate the function of Slc12a8. Based on our results, such compounds could be tested as potential therapeutic agents for age-associated sarcopenia and frailty.

Our results highlight a key role of *Slc12a8* in the LH for regulation of energy metabolism and skeletal muscle functions and imply its importance in the pathogenesis of sarcopenia and frailty during aging.

Limitations of this study

Although our results demonstrate the functional link between *Slc12a8* in the LH and skeletal muscle, which is mediated by the sympathetic nerve-β2AR axis, the neural circuit and the molecular mechanism by which *Slc12a8*-positive neurons in the LH regulate the sympathetic nervous tone directed to skeletal muscle remain unclear. In this regard, further characterization of *Slc12a8*-positive neurons, their projection sites, and their neural activities will be of great importance to better understand the importance of this Slc12a8-mediated inter-tissue communication during aging.

STAR★METHODS

Detailed methods are provided in the online version of this paper and include the following:

- KEY RESOURCES TABLE
- RESOURCE AVAILABILITY
  - Lead contact
  - Materials availability
  - Data and code availability
- EXPERIMENTAL MODEL AND SUBJECT DETAILS
  - Animals
  - Cell culture and primary cell culture
- METHOD DETAILS
  - Stereotaxic injection of lentivirus
  - Metabolic cage analysis
  - Skeletal muscle functional test
  - Histological, immunohistochemical, and RNAscope analysis
  - Laser captured microdissection
  - RNA isolation and reverse transcription-polymerase chain reaction analysis
  - Western blotting
  - Measurement of metabolites
- QUANTIFICATION AND STATISTICAL ANALYSIS

Figure 6. Overexpression of *Slc12a8* in the LH ameliorates age-associated decreases in energy expenditure, endurance capacity, and muscle force

(A–C) Metabolic cage analysis for energy expenditure (A), carbohydrate expenditure (B), and fat expenditure (C) of aged, LH-specific *Slc12a8*-OE mice. n = 14–15.
(D) Rectal temperature of aged, LH-specific *Slc12a8*-OE mice. n = 10.
(E) Endurance capacity of aged, LH-specific *Slc12a8*-OE mice by treadmill analysis. n = 11.
(F and G) Carbohydrate expenditure (F) and fat expenditure (G) at maximum speed of aged, LH-specific *Slc12a8*-OE mice. n = 11.
(H) Twitch force measurement of aged, LH-specific *Slc12a8*-OE mice. n = 12–13.
(I) *In vivo* muscle force-frequency curve of aged, LH-specific *Slc12a8*-OE mice. n = 12–13.
(J) Force reduction during repeated electrical stimulation in aged, LH-specific *Slc12a8*-OE mice. n = 12–13.
*p < 0.05, **p < 0.01, and ***p < 0.001 by Student's t test for (D)–(F) or by two-way repeated-measures ANOVA for (A)–(C) and (I). Error bars indicate SEM.

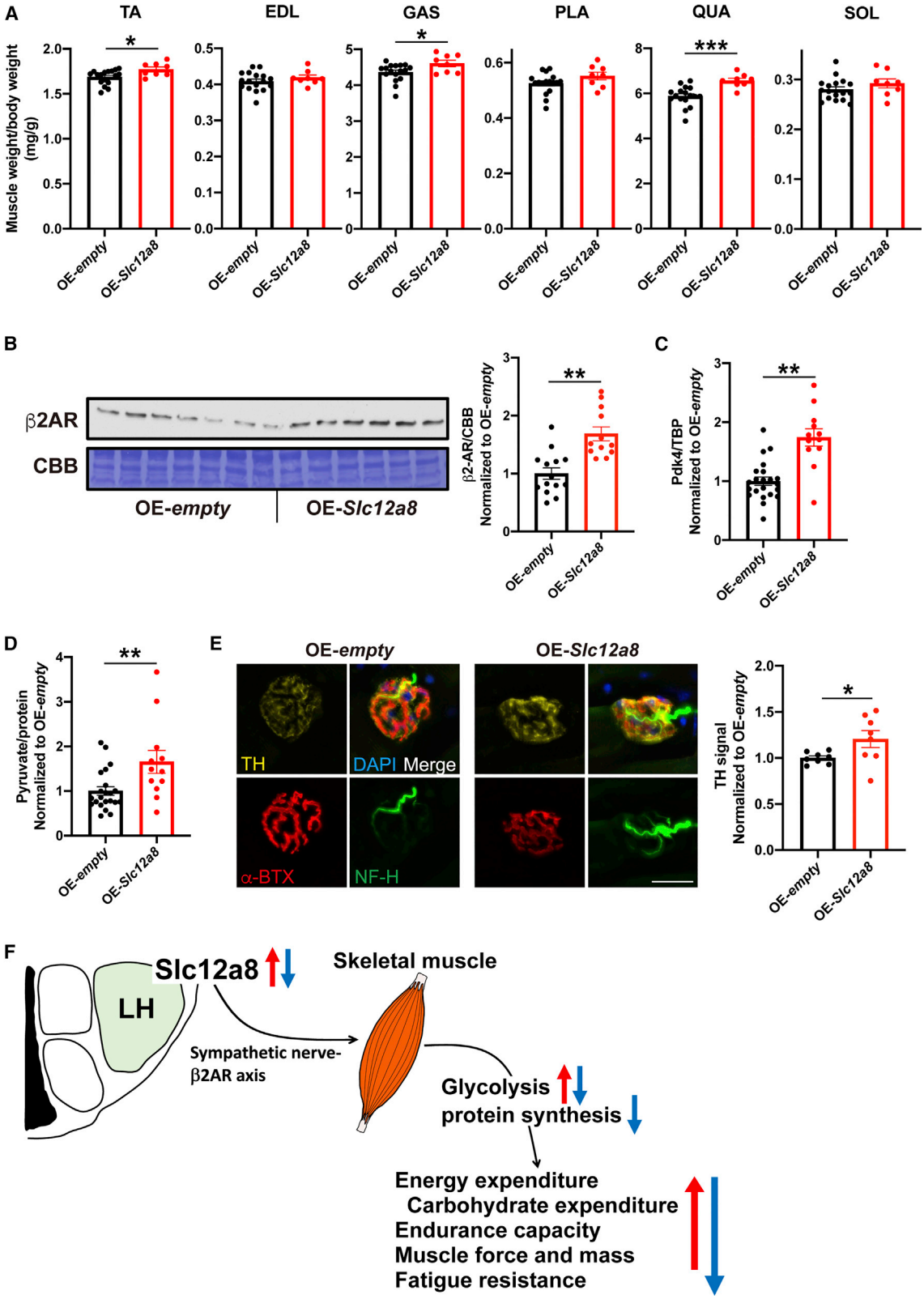

(legend on next page)

SUPPLEMENTAL INFORMATION

Supplemental information can be found online at https://doi.org/10.1016/j.celrep.2022.111131.

ACKNOWLEDGMENTS

We thank Katsuyuki Nakamura (Teijin Limited) for design and construction of *Slc12a8-CreERT2* mice. We also thank Kunio Nakata (Teijin Limited), Isao Kii (Shinshu University), Akiko Satoh (National Center for Geriatrics and Gerontology), and Kyohei Tokizane (Washington University School of Medicine) for valuable discussions and Ken Kanda (SHINFACTORY) and Hitoshi Ishii (ARCO SYSTEM) for technical support for the metabolic cage analysis. This research was supported by a Cyclic Innovation for Clinical Empowerment (CiCLE) grant entitled "Research and Development of Preventive or Therapeutic Drug for Frailty" (grant JP18pc0101021) from the Japan Agency for Medical Research and Development (AMED).

AUTHOR CONTRIBUTIONS

N.I. and S.I. conceived and designed the experiments and wrote the manuscript. S.I. supervised this research project, and N.I. performed most experiments. A.T. performed staining of brain sections, production of lentiviruses, and analysis of NMJs. H.I. analyzed *Slc12a8*-expressing cells. Y. Koike. analyzed *Slc12a8-CreERT2* mice. K.Y. and Y. Kamei performed a long-term (1 month) voluntary running exercise experiment. All authors fully discussed the results and contributed to the manuscript.

DECLARATION OF INTERESTS

The authors declare that there are no conflicts of interest.

Received: January 26, 2022
Revised: May 1, 2022
Accepted: July 1, 2022
Published: July 26, 2022

REFERENCES

Amin, R.H., Mathews, S.T., Camp, H.S., Ding, L., and Leff, T. (2010). Selective activation of PPARgamma in skeletal muscle induces endogenous production of adiponectin and protects mice from diet-induced insulin resistance. Am. J. Physiol. Endocrinol. Metab. *298*, E28–E37. https://doi.org/10.1152/ajpendo.00446.2009.

Atas, E., Oberhuber, M., and Kenner, L. (2020). The implications of PDK1-4 on tumor energy metabolism, aggressiveness and therapy resistance. Front. Oncol. *10*, 583217. https://doi.org/10.3389/fonc.2020.583217.

Bentzinger, C.F., Romanino, K., Cloëtta, D., Lin, S., Mascarenhas, J.B., Oliveri, F., Xia, J., Casanova, E., Costa, C.F., Brink, M., et al. (2008). Skeletal muscle-specific ablation of raptor, but not of rictor, causes metabolic changes and results in muscle dystrophy. Cell Metab. *8*, 411–424. https://doi.org/10.1016/j.cmet.2008.10.002.

Caglar, C., and Friedman, J. (2021). Restriction of food intake by PPP1R17-expressing neurons in the DMH. Proc. Natl. Acad. Sci. USA *118*, e2100194118. https://doi.org/10.1073/pnas.2100194118.

Cesari, M., Landi, F., Vellas, B., Bernabei, R., and Marzetti, E. (2014). Sarcopenia and physical frailty: two sides of the same coin. Front. Aging Neurosci. *6*, 192. https://doi.org/10.3389/fnagi.2014.00192.

Cetin, A., Komai, S., Eliava, M., Seeburg, P.H., and Osten, P. (2006). Stereotaxic gene delivery in the rodent brain. Nat. Protoc. *1*, 3166–3173. https://doi.org/10.1038/nprot.2006.450.

Chen, S., Minegishi, Y., Hasumura, T., Shimotoyodome, A., and Ota, N. (2020). Involvement of ammonia metabolism in the improvement of endurance performance by tea catechins in mice. Sci. Rep. *10*, 6065. https://doi.org/10.1038/s41598-020-63139-9.

Chini, C.C.S., Zeidler, J.D., Kashyap, S., Warner, G., and Chini, E.N. (2021). Evolving concepts in NAD(+) metabolism. Cell Metab. *33*, 1076–1087. https://doi.org/10.1016/j.cmet.2021.04.003.

Chinsomboon, J., Ruas, J., Gupta, R.K., Thom, R., Shoag, J., Rowe, G.C., Sawada, N., Raghuram, S., and Arany, Z. (2009). The transcriptional coactivator PGC-1alpha mediates exercise-induced angiogenesis in skeletal muscle. Proc. Natl. Acad. Sci. USA *106*, 21401–21406. https://doi.org/10.1073/pnas.0909131106.

Conte, T.C., Silva, L.H., Silva, M.T., Hirabara, S.M., Oliveira, A.C., Curi, R., Moriscot, A.S., Aoki, M.S., and Miyabara, E.H. (2012). The beta2-adrenoceptor agonist formoterol improves structural and functional regenerative capacity of skeletal muscles from aged rat at the early stages of postinjury. J. Gerontol. A. Biol. Sci. Med. Sci. *67*, 443–455. https://doi.org/10.1093/gerona/glr195.

Dao, T., Green, A.E., Kim, Y.A., Bae, S.J., Ha, K.T., Gariani, K., Lee, M.R., Menzies, K.J., and Ryu, D. (2020). Sarcopenia and muscle aging: a brief overview. Endocrinol. Metab. *35*, 716–732. https://doi.org/10.3803/EnM.2020.405.

Egerman, M.A., and Glass, D.J. (2014). Signaling pathways controlling skeletal muscle mass. Crit. Rev. Biochem. Mol. Biol. *49*, 59–68. https://doi.org/10.3109/10409238.2013.857291.

Fang, E.F., Hou, Y., Palikaras, K., Adriaanse, B.A., Kerr, J.S., Yang, B., Lautrup, S., Hasan-Olive, M.M., Caponio, D., Dan, X., et al. (2019). Mitophagy inhibits amyloid-beta and tau pathology and reverses cognitive deficits in models of Alzheimer's disease. Nat. Neurosci. *22*, 401–412. https://doi.org/10.1038/s41593-018-0332-9.

Fang, E.F., Scheibye-Knudsen, M., Brace, L.E., Kassahun, H., SenGupta, T., Nilsen, H., Mitchell, J.R., Croteau, D.L., and Bohr, V.A. (2014). Defective mitophagy in XPA via PARP-1 hyperactivation and NAD(+)/SIRT1 reduction. Cell *157*, 882–896. https://doi.org/10.1016/j.cell.2014.03.026.

Gan, Z., Burkart-Hartman, E.M., Han, D.H., Finck, B., Leone, T.C., Smith, E.Y., Ayala, J.E., Holloszy, J., and Kelly, D.P. (2011). The nuclear receptor PPARbeta/delta programs muscle glucose metabolism in cooperation with AMPK and MEF2. Genes. Dev. *25*, 2619–2630. https://doi.org/10.1101/gad.178434.111.

Goodman, C.A., and Hornberger, T.A. (2013). Measuring protein synthesis with SUnSET: a valid alternative to traditional techniques? Exerc. Sport. Sci. Rev. *41*, 107–115. https://doi.org/10.1097/JES.0b013e3182798a95.

Grozio, A., Mills, K.F., Yoshino, J., Bruzzone, S., Sociali, G., Tokizane, K., Lei, H.C., Cunningham, R., Sasaki, Y., Migaud, M.E., and Imai, S.I. (2019). Slc12a8 is a nicotinamide mononucleotide transporter. Nat. Metab. *1*, 47–57. https://doi.org/10.1038/s42255-018-0009-4.

Grygiel-Górniak, B. (2014). Peroxisome proliferator-activated receptors and their ligands: nutritional and clinical implications–a review. Nutr. J. *13*, 17. https://doi.org/10.1186/1475-2891-13-17.

Figure 7. Overexpression of *Slc12a8* in the LH ameliorates age-associated decreases in tissue and molecular phenotypes in skeletal muscle

(A) Hindlimb muscle weights of aged, LH-specific *Slc12a8*-OE mice. n = 8–17.

(B) Representative western blotting for β2AR (left) and its quantitative analysis in aged, LH-specific *Slc12a8*-OE mice (right). n = 12–14.

(C) mRNA expression levels of *PDK4* in aged, LH-specific *Slc12a8*-OE mice. n = 12–22.

(D) Amounts of pyruvate in aged, LH-specific *Slc12a8*-OE mice. n = 12–22.

(E) Representative images of TH (a marker of the sympathetic nerve, yellow), α-BTX (a marker of NMJs, red), and NF-H (a marker of motor neurons, green) in aged, LH-specific *Slc12a8*-OE mice (left) and quantitative analysis of TH signals around NMJs in aged, LH-specific *Slc12a8*-OE mice (right). n = 8.

(F) A schematic for Slc12a8-mediated regulation of skeletal muscle function in the LH during aging.

*p < 0.05, **p < 0.01, and ***p < 0.001 by Student's t test. Error bars indicate SEM.

Ham, D.J., Börsch, A., Lin, S., Thürkauf, M., Weihrauch, M., Reinhard, J.R., Delezie, J., Battilana, F., Wang, X., Kaiser, M.S., et al. (2020). The neuromuscular junction is a focal point of mTORC1 signaling in sarcopenia. Nat. Commun. *11*, 4510. https://doi.org/10.1038/s41467-020-18140-1.

Hong, F., Pan, S., Guo, Y., Xu, P., and Zhai, Y. (2019). PPARs as nuclear receptors for nutrient and energy metabolism. Molecules *24*, E2545. https://doi.org/10.3390/molecules24142545.

Ito, N., Kii, I., Shimizu, N., Tanaka, H., and Takeda, S. (2017). Direct reprogramming of fibroblasts into skeletal muscle progenitor cells by transcription factors enriched in undifferentiated subpopulation of satellite cells. Sci. Rep. *7*, 8097. https://doi.org/10.1038/s41598-017-08232-2.

Ito, N., Ruegg, U.T., Kudo, A., Miyagoe-Suzuki, Y., and Takeda, S. (2013). Activation of calcium signaling through Trpv1 by nNOS and peroxynitrite as a key trigger of skeletal muscle hypertrophy. Nat. Med. *19*, 101–106. https://doi.org/10.1038/nm.3019.

Ito, N., Ruegg, U.T., and Takeda, S. (2018). ATP-induced increase in intracellular calcium levels and subsequent activation of mTOR as regulators of skeletal muscle hypertrophy. Int. J. Mol. Sci. *19*, E2804. https://doi.org/10.3390/ijms19092804.

Johnson, S., Wozniak, D.F., and Imai, S. (2018). CA1 Nampt knockdown recapitulates hippocampal cognitive phenotypes in old mice which nicotinamide mononucleotide improves. NPJ Aging Mech. Dis. *4*, 10. https://doi.org/10.1038/s41514-018-0029-z.

Katsyuba, E., Romani, M., Hofer, D., and Auwerx, J. (2020). NAD(+) homeostasis in health and disease. Nat. Metab. *2*, 9–31. https://doi.org/10.1038/s42255-019-0161-5.

Khan, M.M., Lustrino, D., Silveira, W.A., Wild, F., Straka, T., Issop, Y., O'Connor, E., Cox, D., Reischl, M., Marquardt, T., et al. (2016). Sympathetic innervation controls homeostasis of neuromuscular junctions in health and disease. Proc. Natl. Acad. Sci. USA *113*, 746–750. https://doi.org/10.1073/pnas.1524272113.

Kim, T.N., and Choi, K.M. (2013). Sarcopenia: definition, epidemiology, and pathophysiology. J. Bone Metab. *20*, 1–10. https://doi.org/10.11005/jbm.2013.20.1.1.

Krämer, D.K., Al-Khalili, L., Perrini, S., Skogsberg, J., Wretenberg, P., Kannisto, K., Wallberg-Henriksson, H., Ehrenborg, E., Zierath, J.R., and Krook, A. (2005). Direct activation of glucose transport in primary human myotubes after activation of peroxisome proliferator-activated receptor delta. Diabetes *54*, 1157–1163. https://doi.org/10.2337/diabetes.54.4.1157.

Liu, Z., Chen, X., Wang, Y., Peng, H., Wang, Y., Jing, Y., and Zhang, H. (2014). PDK4 protein promotes tumorigenesis through activation of cAMP-response element-binding protein (CREB)-Ras homolog enriched in brain (RHEB)-mTORC1 signaling cascade. J. Biol. Chem. *289*, 29739–29749. https://doi.org/10.1074/jbc.M114.584821.

Madisen, L., Zwingman, T.A., Sunkin, S.M., Oh, S.W., Zariwala, H.A., Gu, H., Ng, L.L., Palmiter, R.D., Hawrylycz, M.J., Jones, A.R., et al. (2010). A robust and high-throughput Cre reporting and characterization system for the whole mouse brain. Nat. Neurosci. *13*, 133–140. https://doi.org/10.1038/nn.2467.

Mills, K.F., Yoshida, S., Stein, L.R., Grozio, A., Kubota, S., Sasaki, Y., Redpath, P., Migaud, M.E., Apte, R.S., Uchida, K., et al. (2016). Long-Term Administration of Nicotinamide Mononucleotide Mitigates Age-Associated Physiological Decline in Mice. Cell Metab *24*, 795–806.

Minegishi, Y., Otsuka, A., Ota, N., Ishii, K., and Shimotoyodome, A. (2018). Combined supplementation of pre-exercise carbohydrate, alanine, and proline and continuous intake of green tea catechins effectively boost endurance performance in mice. Nutrients *10*, E925. https://doi.org/10.3390/nu10070925.

Myers, M.J., Shepherd, D.L., Durr, A.J., Stanton, D.S., Mohamed, J.S., Hollander, J.M., and Alway, S.E. (2019). The role of SIRT1 in skeletal muscle function and repair of older mice. J. Cachexia Sarcopenia Muscle *10*, 929–949. https://doi.org/10.1002/jcsm.12437.

Okamoto, S., Sato, T., Tateyama, M., Kageyama, H., Maejima, Y., Nakata, M., Hirako, S., Matsuo, T., Kyaw, S., Shiuchi, T., et al. (2018). Activation of AMPK-regulated CRH neurons in the PVH is sufficient and necessary to induce dietary preference for carbohydrate over fat. Cell Rep. *22*, 706–721. https://doi.org/10.1016/j.celrep.2017.11.102.

Pearen, M.A., Myers, S.A., Raichur, S., Ryall, J.G., Lynch, G.S., and Muscat, G.E.O. (2008). The orphan nuclear receptor, NOR-1, a target of beta-adrenergic signaling, regulates gene expression that controls oxidative metabolism in skeletal muscle. Endocrinology *149*, 2853–2865. https://doi.org/10.1210/en.2007-1202.

Rahimi, Y., Camporez, J.P.G., Petersen, M.C., Pesta, D., Perry, R.J., Jurczak, M.J., Cline, G.W., and Shulman, G.I. (2014). Genetic activation of pyruvate dehydrogenase alters oxidative substrate selection to induce skeletal muscle insulin resistance. Proc. Natl. Acad. Sci. USA *111*, 16508–16513. https://doi.org/10.1073/pnas.1419104111.

Rajman, L., Chwalek, K., and Sinclair, D.A. (2018). Therapeutic potential of NAD-boosting molecules: the in vivo evidence. Cell Metab. *27*, 529–547. https://doi.org/10.1016/j.cmet.2018.02.011.

Rodrigues, A.C.Z., Messi, M.L., Wang, Z.M., Abba, M.C., Pereyra, A., Birbrair, A., Zhang, T., O'Meara, M., Kwan, P., Lopez, E.I.S., et al. (2019). The sympathetic nervous system regulates skeletal muscle motor innervation and acetylcholine receptor stability. Acta Physiol. *225*, e13195. https://doi.org/10.1111/apha.13195.

Ryall, J.G., Plant, D.R., Gregorevic, P., Sillence, M.N., and Lynch, G.S. (2004). Beta 2-agonist administration reverses muscle wasting and improves muscle function in aged rats. J. Physiol. *555*, 175–188. https://doi.org/10.1113/jphysiol.2003.056770.

Santulli, G., and Iaccarino, G. (2013). Pinpointing beta adrenergic receptor in ageing pathophysiology: victim or executioner? Evidence from crime scenes. Immun. Ageing *10*, 10. https://doi.org/10.1186/1742-4933-10-10.

Satoh, A., Brace, C.S., Rensing, N., Cliften, P., Wozniak, D.F., Herzog, E.D., Yamada, K.A., and Imai, S. (2013). Sirt1 extends life span and delays aging in mice through the regulation of Nk2 homeobox 1 in the DMH and LH. Cell Metab. *18*, 416–430. https://doi.org/10.1016/j.cmet.2013.07.013.

Schertzer, J.D., Plant, D.R., Ryall, J.G., Beitzel, F., Stupka, N., and Lynch, G.S. (2005). Beta2-agonist administration increases sarcoplasmic reticulum Ca2+-ATPase activity in aged rat skeletal muscle. Am. J. Physiol. Endocrinol. Metab. *288*, E526–E533. https://doi.org/10.1152/ajpendo.00399.2004.

Shimizu, N., Maruyama, T., Yoshikawa, N., Matsumiya, R., Ma, Y., Ito, N., Tasaka, Y., Kuribara-Souta, A., Miyata, K., Oike, Y., et al. (2015). A muscle-liver-fat signalling axis is essential for central control of adaptive adipose remodelling. Nat. Commun. *6*, 6693. https://doi.org/10.1038/ncomms7693.

Shiuchi, T., Haque, M.S., Okamoto, S., Inoue, T., Kageyama, H., Lee, S., Toda, C., Suzuki, A., Bachman, E.S., Kim, Y.B., et al. (2009). Hypothalamic orexin stimulates feeding-associated glucose utilization in skeletal muscle via sympathetic nervous system. Cell Metab. *10*, 466–480. https://doi.org/10.1016/j.cmet.2009.09.013.

Snyder-Warwick, A.K., Satoh, A., Santosa, K.B., Imai, S., and Jablonka-Shariff, A. (2018). Hypothalamic Sirt1 protects terminal Schwann cells and neuromuscular junctions from age-related morphological changes. Aging Cell *17*, e12776. https://doi.org/10.1111/acel.12776.

Straka, T., Vita, V., Prokshi, K., Hörner, S.J., Khan, M.M., Pirazzini, M., Williams, M.P.I., Hafner, M., Zaglia, T., and Rudolf, R. (2018). Postnatal development and distribution of sympathetic innervation in mouse skeletal muscle. Int. J. Mol. Sci. *19*, E1935. https://doi.org/10.3390/ijms19071935.

Stuber, G.D., and Wise, R.A. (2016). Lateral hypothalamic circuits for feeding and reward. Nat. Neurosci. *19*, 198–205. https://doi.org/10.1038/nn.4220.

Talbot, J., and Maves, L. (2016). Skeletal muscle fiber type: using insights from muscle developmental biology to dissect targets for susceptibility and resistance to muscle disease. Wiley Interdiscip. Rev. Dev. Biol. *5*, 518–534. https://doi.org/10.1002/wdev.230.

Verdin, E. (2015). NAD(+) in aging, metabolism, and neurodegeneration. Science *350*, 1208–1213. https://doi.org/10.1126/science.aac4854.

Wagenmakers, A.J. (1998). Muscle amino acid metabolism at rest and during exercise: role in human physiology and metabolism. Exerc. Sport. Sci. Rev. *26*, 287–314.

Xiao, X., Yeghiazaryan, G., Hess, S., Klemm, P., Sieben, A., Kleinridders, A., Morgan, D.A., Wunderlich, F.T., Rahmouni, K., Kong, D., et al. (2021). Orexin receptors 1 and 2 in serotonergic neurons differentially regulate peripheral glucose metabolism in obesity. Nat. Commun. *12*, 5249. https://doi.org/10.1038/s41467-021-25380-2.

Yoon, M.S. (2017). The role of mammalian target of rapamycin (mTOR) in insulin signaling. Nutrients *9*, E1176. https://doi.org/10.3390/nu9111176.

Yoshino, J., Baur, J.A., and Imai, S. (2018). NAD(+) intermediates: the biology and therapeutic potential of NMN and NR. Cell Metab. *27*, 513–528. https://doi.org/10.1016/j.cmet.2017.11.002.

Yoshino, M., Yoshino, J., Kayser, B.D., Patti, G.J., Franczyk, M.P., Mills, K.F., Sindelar, M., Pietka, T., Patterson, B.W., Imai, S.I., and Klein, S. (2021). Nicotinamide mononucleotide increases muscle insulin sensitivity in prediabetic women. Science *372*, 1224–1229.

STAR★METHODS

KEY RESOURCES TABLE

REAGENT or RESOURCE	SOURCE	IDENTIFIER
Antibodies		
Anti-ZsGreen	FRONTIER INSTITUTE	ZsGreen-Rb RRID:AB_2571858
Anti-Orexin	CST	#16743; RRID:AB_10013632
Anti-MCH	PHOENIX PHARMACEUTICALS	H-070-47; RRID:AB_10013632
Anti-GFP	NACALAI TESQUE	04,404–84; RRID:AB_10013361
Anti-PPP1r17	Thermo Fisher Scientific	PA5-61599; RRID:AB_2645859
Anti-p-p70S6K (Thr389)	CST	#9205; RRID:AB_330944
Anti-p-p70S6K (Thr421/Ser424)	CST	#9204; RRID:AB_2265913
Anti-p70S6K	CST	#2708; RRID:AB_390722
Anti-p-S6 (Ser235/236)	CST	#4858; RRID:AB_916156
Anti-p-S6 (Ser240/244)	CST	#5364; RRID:AB_10694233
Anti-S6	CST	#2217; RRID:AB_331355
Anti-p-Akt (Ser473)	CST	#9271; RRID:AB_329825
Anti-p-Akt (Thr308)	CST	#13038; RRID:AB_2629447
Anti-Akt	CST	#9272; RRID:AB_329827
anti-p-FoxO1 (Ser256)	CST	#9461; RRID:AB_329831
anti-FoxO1	CST	#2880; RRID:AB_2106495
anti-p-FoxO3a (Ser253)	CST	#13129; RRID:AB_2687495
anti-FoxO3a	CST	#12829; RRID:AB_2636990
Anti-puromycin	Millipore	MABE343; RRID:AB_2566826
Anti-p-PDH (Ser293)	NOVUS	NB110-93479; RRID:AB_1237282
Anti-PDH	Abcam	8D10 × 10^6; RRID:AB_2533825
Anti-Adrb2	Abcam	ab182136; RRID:AB_2747383
Anti-Tyrosine hydroxylase	MERCK	AB152; RRID:AB_390204
Anti-Neurofilament H	Biolegend	801,701; RRID:AB_2564642
Anti-α-tubulin	CST	#3873; RRID:AB_1904178
Anti-BA-D5	Developmental Studies Hybridoma Bank	BA-D5; RRID:AB_2235587
Anti-SC-71	Developmental Studies Hybridoma Bank	SC-71; RRID:AB_2147165
Anti-BF-F3	Developmental Studies Hybridoma Bank	BF-F3; RRID:AB_2266724
Anti Laminin α2	Enzo Life Sciences	ALX-804-190-C100; RRID:AB_2051764
Anti-IgG, Mouse, Goat-Poly, HRP, EasyBlot	GeneTex	GTX221667-01; RRID:AB_10728926
Anti-Rabbit IgG, HRP-Linked F(ab')2 Fragment Donkey	GE	NA9340-1ML; RRID:AB_772191
Goat anti-Rabbit IgG (H + L) Cross-Adsorbed Secondary Antibody, Alexa Fluor 488	ThermoFisher	A-11008; RRID:AB_143165
Goat anti-Rabbit IgG (H + L) Cross-Adsorbed Secondary Antibody, Alexa Fluor 555	ThermoFisher	A-21428; RRID:AB_2535849
Goat anti-Rat IgG (H + L) Cross-Adsorbed Secondary Antibody, Alexa Fluor 488	ThermoFisher	A-11006; RRID:AB_2534074
Goat anti-Mouse IgG1 Cross-Adsorbed Secondary Antibody, Alexa Fluor 488	ThermoFisher	A-21121; RRID:AB_2535764
Goat anti-Mouse IgM (Heavy chain) Cross-Adsorbed Secondary Antibody, Alexa Fluor 555	ThermoFisher	A-21426; RRID:AB_2535847

(*Continued on next page*)

Continued

REAGENT or RESOURCE	SOURCE	IDENTIFIER
Goat anti-Mouse IgG2b Cross-Adsorbed Secondary Antibody, Alexa Fluor 555	ThermoFisher	A-21147; RRID:AB_2535783
Goat anti-Mouse IgG1 Cross-Adsorbed Secondary Antibody, Alexa Fluor 555	ThermoFisher	A-21127; RRID:AB_2535769
Bacterial and virus strains		
sh-*fLuc*	This study	N/A
sh-*Slc12a8*	This study	N/A
OE-*empty*	This study	N/A
OE-*Slc12a8*	This study	N/A
sh-*Nampt*	This study	N/A
sh-*Pdk4*	This study	N/A
Chemicals, peptides, and recombinant proteins		
Tamoxifen	Sigma-Aldrich	T5648
DAPI	NACALAI TESQUE	11,034–56
Slc12a8 probe	Advanced Cell Diagnostics	846,731
Slc12a8 probe	Advanced Cell Diagnostics	846,551
Slc32a1 probe	Advanced Cell Diagnostics	319,191
Slc17a6 probe	Advanced Cell Diagnostics	319,171
Cre probe	Advanced Cell Diagnostics	312,281
Alexa 647 conjugated-α-BTX	Thermo Fisher Scientific	B35450
Puromycin	NACALAI TESQUE	29,455–12
βFGF	peprotech	450–33
TRIzol	Thermo Fisher Scientific	15,596,018
FK866	Toronto Research Chemicals Inc.	F370030
Sucrose	NACALAI TESQUE	30,404–45
HEPES	FUJIFILM Wako Pure Chemical Corporation	346–01,373
EGTA	NACALAI TESQUE	890,742
EDTA	NACALAI TESQUE	08,907–42
$Na_4P_2O_7$	FUJIFILM Wako Pure Chemical Corporation	195–03,025
NaF	NACALAI TESQUE	3,142,082
Glycerophosphate	Sigma-Aldrich	G9422
Na_3VO_4	FUJIFILM Wako Pure Chemical Corporation	198–09,752
Glycerol	NACALAI TESQUE	17,017–35
Tris	NACALAI TESQUE	35,434–05
SDS	NACALAI TESQUE	31,606–75
β-mercaptoethanol	NACALAI TESQUE	21,417–52
Bromophenol blue	NACALAI TESQUE	580,861
Tween 20	FUJIFILM Wako Pure Chemical Corporation	167–11,515
paraformaldehyde	Electron Microscopy Science	15,710
BSA	Sigma-Aldrich	A9418
Critical commercial assays		
Glycogen Assay kit	BioVision	K646-100
Pyruvate Assay kit	BioVision	K609-100
NAD/NADH-Glo	Promega	G9071
PicoPure RNA Isolation Kit	Applied Biosystem	KIT0204

(*Continued on next page*)

Continued

REAGENT or RESOURCE	SOURCE	IDENTIFIER
PureLink DNase Set	Thermo Fisher Scientific	12,185,010
TransIT®-Lenti Transfection Reagent	TAKARA BIO	V6604
Lenti-X™ Maxi Purification Kit	TAKARA BIO	Z1234N
Lenti-X™ qRT-PCR Titration Kit	TAKARA BIO	Z1235N
RNAscope Multiplex Fluorescent Reagent Kit v2	Advanced Cell Diagnostics	323,100
TB Green® Premix Ex Taq™ II (Tli RNaseH Plus)	TAKARA BIO	RR820B
SuperScript™ IV VILO™ Master Mix with ezDNase™ Enzyme	Thermo Fisher Scientific	11,766,050
ECL Western blotting detection reagents	GE	RPN2106
CBB Stain One Super	NACALAI TESQUE	11,642–31
DMEM	GIBCO	10,569–010
DMEM	Sigma-Aldrich	D6429-500ML
ProLong Glass Antifade Mountant	Thermo Fisher Scientific	P36984
LAB Gluco	ForaCare Japan	4239R1006
cOmplete, Mini Protease Inhibitor Cocktail	Merck	11,836,153,001
Matrigel	BD	356,237
goat serum	Cedarlane	CL1200
KOD FX	TOYOBO	KFX-101
Bradford protein assay dye reagent concentrate	Bio-Rad	5000006JA
Experimental models: Cell lines		
Primary myoblast	This paper	N/A
Lenti-X 293T	TAKARA BIO	Z2180N
Neuro2a	ACTT	CCL-131
Experimental models: Organisms/strains		
C57BL6/j	Oriental Yeast	N/A
Slc12a8-CreERT2 mice	This paper	N/A
B6.Cg-Gt(ROSA)26Sortm6 (CAG-ZsGreen1) Hze/J	Jackson Labratory	#007906
Oligonucleotides		
Ppara f: 5′-agaagttgcaggaggggatt-3′	This paper	N/A
Ppara r: 5′-ttgaaggagctttgggaaga-3′	This paper	N/A
Ppard f: 5′-gatggaagaccactcgcatt-3′	This paper	N/A
Ppard r: 5′-aaccattgggtcagctcttg-3′	This paper	N/A
Pparg f: 5′-gatggaagaccactcgcatt-3′	This paper	N/A
Pparg r: 5′-aaccattgggtcagctcttg-3′	This paper	N/A
Pdk4 f: 5′-tgactcaaagacgggaaacc-3′	This paper	N/A
Pdk4 r: 5′-actggtcgcagagcatcttt-3′	This paper	N/A
Trim63 f: 5′-atggagaacctggagaagcagc-3′	This paper	N/A
Trim63 r: 5′-tggaagatgtcgttggcacac-3′	This paper	N/A
Fbxo32 f: 5′-ccagcacacgacaacacttcag-3′	This paper	N/A
Fbxo32 r: 5′-tatcccccgcagtttcaagc-3′	This paper	N/A
Slc12a8 f: 5′-ggcggtgtctactccatgat-3′	This paper	N/A
Slc12a8 r: 5′-agcacctgcaacacactgtc-3′	This paper	N/A
GAPDH f: 5′-acccagaagactgtggatgg-3′	This paper	N/A
GAPDH r: 5′-ggatgcagggatgatgttct-3′	This paper	N/A
Tbp f: 5′-cagcctcagtacagcaatcaac-3′	This paper	N/A

(*Continued on next page*)

Continued

REAGENT or RESOURCE	SOURCE	IDENTIFIER
Tbp r: 5′-taggggtcataggagtcattgg-3′	This paper	N/A
Software and algorithms		
ImageJ	FIJI	https://imagej.net/software/fiji/
GraphPad Prism 8, version 8.4.3	GrapPad	RRID: SCR-002798
Other		
Hyperfilm ECL	GE	28-9068-39

RESOURCE AVAILABILITY

Lead contact

- Further information and requests for resources and reagents should be directed to and will be fulfilled by the lead contact, Shin-ichiro Imai (imaishin@wustl.edu).

Materials availability

- Mice generated in this study are available from the lead contact with a Materials Transfer Agreement.

Data and code availability

- Upon reasonable request, any data reported in this paper are available from the lead contact.
- This paper does not report original code.
- Any additional information required to reanalyze the data reported in this paper is available from the lead contact upon request.

EXPERIMENTAL MODEL AND SUBJECT DETAILS

Animals

C57BL/6 mice were purchased from Oriental Yeast Co., Ltd. (Tokyo, Japan). *Slc12a8-CreERT2* mice were generated at the Transborder Medical Research Center in Tsukuba University. *Rosa26-CAG-LSL-ZsGreen* mice were from Jackson Laboratory (Madisen et al., 2010). All mice were housed at the institutional animal facility in National Cerebral and Cardiovascular Center or in RIKEN on a 12 h:12 h light/dark cycle. All animal procedures were approved by the Experimental Animal Care and Use Committee at the National Cerebral and Cardiovascular Center (Approval number: 19,051, 21,045, 21,066, 21,067), or at the Foundation for Biomedical Research and Innovation at Kobe (FBRI) (Approval number: 18-01). Male mice were used for analysis. Young, middle aged and aged mice were defined as 3-4 months, 18-20 months and 26-28-months-old, respectively. All experimental methods were performed in accordance with approved guidelines.

Cell culture and primary cell culture

Neuro2a cells were purchased from ATCC. The cells were maintained with DMEM (high glucose, 4 mM L-glutamine, sodium bicarbonate, and sodium pyruvate, Sigma-Aldrich, D6429) supplemented with 10% fetal bovine serum (FBS) and 1% penicillin-streptomycin (Thermo Fisher) at 37°C with 5% CO_2.

Primary culture of muscle progenitor cells was performed as described previously with minor modifications (Ito et al., 2017). Briefly, EDL muscles from 3-4-months old mice were dissociated with 0.2% type 1 collagenase (Worthington)/DMEM for 90 min. After gentle pipetting of dissociated muscles, muscle fibers were isolated and plated on Matrigel (Matrigel-Growth Factor Reduced, BD Biosciences)-coated dishes. Isolated muscle fibers with primary muscle progenitor cells were cultured in DMEM (high glucose, sodium pyruvate, and GlutaMAX supplement; Thermo Fisher Scientific) supplemented with 20% FBS, 2.5 ng/mL of basic fibroblast growth factor , and 1% penicillin-streptomycin (Thermo Fisher) at 37°C with 5% CO_2. The medium was changed every 2 days. Differentiation was induced by replacing medium to DMEM supplemented with 10% FBS and 1% penicillin-streptomycin.

METHOD DETAILS

Stereotaxic injection of lentivirus

Stereotaxic injection of lentivirus into the LH was performed as described previously with minor modification (Cetin et al., 2006; Grozio et al., 2019; Satoh et al., 2013). Briefly, young and middle-aged mice were anesthetized with 1.5% and 1.0% isoflurane, respectively, with a temperature-regulated incubator. The mice were placed in a three-point fixation stereotaxic frame (model 963, David Kopf Instruments). A midline incision was made, and the periosteum was dissected from the cranium. Appropriate coordinates for the stereotaxic injection were registered: relative to bregma, anterior-posterior −1.8 mm, medial-lateral ± 0.9 mm,

and dorsal-ventral −5.4 mm. Hamilton microsyringe (Neuros Model 7000.5 KH) was directed to the indicated coordinate. The solution containing lentivirus was slowly injected (0.1 μL/min) using an electrical syringe pump (Legato 130). Total volume of lentivirus solution was 0.4 μL. Lentivirus with a titer of 2.0–3.5 x 10^{10} genome copy/mL was used for stereotaxic injection. The incision was closed with 7-0 nylon sutures. All injected mice had one week to recover before being used for experiments. Three months after the injection of lentivirus, the functional and biological tests were performed.

Lentivirus was produced as described previously with modifications (Grozio et al., 2019; Ito et al., 2017). Briefly, TransIT-Lenti Transfection Reagent (Takara) were used for lentivirus preparation. The produced lentivirus was collected 3 days after transfection and was purified by Lenti-X Maxi Purification Kit (Takara). The titer of lentivirus was analyzed by Lenti-X qRT-PCR Titration Kit (Takara).

Metabolic cage analysis

Metabolic cage analysis were performed as described previously with modification (Chen et al., 2020; Okamoto et al., 2018). Briefly, food intake, activity in the cage, and running distance using a running wheel were measured with the use of a feeding and activity monitoring system (MFD-RQ, SHINFACTORY). Movement in the cage was measured by a beam sensor. All animals were habituated to the metabolic cage for 3 days before experiments. The average of the cumulative data from 4 to 7 days was used. Energy metabolism was analyzed using an ARCO-2000 magnetic-type mass spectrometric calorimeter (ARCO SYSTEMS). Oxygen consumption (VO_2) and carbon dioxide exhalation (VCO_2) were measured. In addition, RER, carbohydrate expenditure, fat expenditure, and energy expenditure were calculated by equations described previously (Minegishi et al., 2018). The average of the data from 4 to 7 days was used. The data were obtained every 5 min.

The rectal temperature at ZT15:00 was analyzed by KN-91-AD1687 (Natsume Seisakusho Co, Ltd, Tokyo, Japan).

Skeletal muscle functional test

The treadmill exercise experimental model was performed as described previously with minor modification (Ito et al., 2018). Briefly, the mice were placed on a flat MB-2000 treadmill (ARCO SYSTEM, Japan) at around ZT15:00. For the first 5 min, the mice were forced to run at 5 m/min. Then, the speed was increased by 1 m/min every minute for 20 min. After the speed reached 25 m/min, the mice were forced to run at constant speed until the mice could not run. In parallel with the endurance test, energy metabolism was analyzed using an ARCO-2000. VO_2, VCO_2, RER, carbohydrate expenditure, fat expenditure, and energy expenditure were measured and calculated. The data were obtained every 2 min.

In vivo muscle force measurement was performed as described previously with modification (Myers et al., 2019). The plantar flexor force and fatigue resistance were analyzed using 1300A (Aurora scientific, ON, Canada). The young and middle-aged mice were anesthetized with 1.5% and 1.0% isoflurane, respectively, and a heated plate was used to maintain body temperature. Hindlimb ankles were positioned at 90° flexion. Muscle force measures were obtained through indirect electrical stimulation of the plantar flexor muscles through the tibial nerve. First, electrically evoked contraction with a single 0.2 msec pulse was measured as twitch force. After 2 min rest, 20, 40, 60, 80, 100, 120, 150, and 200 Hz for 0.35 s with 1 min interval was applied to analyze force-frequency curve. After 2 min rest, a fatigue resistance test was performed with 60 repeated electrical stimulations with a 2 s interval of 30 Hz for 0.35 s. The reduction from maximum to minimum muscle force was calculated as % reduction.

Histological, immunohistochemical, and RNAscope analysis

Histological and immunohistochemical analyses were performed as described previously with minor modifications (Ito et al., 2013, 2017; Snyder-Warwick et al., 2018).

For immunohistochemical analysis of the brain, the mice were anesthetized and perfused with 4% paraformaldehyde (Electron Microscopy Science, Hatfield, PA, USA) (PFA)/PBS. The isolated brain was postfixed overnight at 4°C, then transferred to 15% sucrose/PBS and 30% sucrose/PBS for cryoprotection, and embedding in OCT (Tissue-Tek, Miles, Elkhart, USA). The 25 μm-thick frozen sections were prepared by a cryostat. The sections were washed with PBS, then permeabilized with 0.3% Triton X-100/PBS for 3 min at room temperature. After washing with PBS, the sections were blocked with 5% goat serum in 1% BSA/0.3% Triton X-100/PBS for 1 h at room temperature followed by staining with the primary antibody in 1% BSA/0.3% Triton X-100/PBS for overnight at 4°C. Anti-ZsGreen (FRONTIER INSTITUTE, MSFR106450, 1:200), anti-orexin (CST, #16743, 1:200), anti-MCH (PHOENIX PHARMACEUTICALS, H-070-47, 1:1000), anti-GFP (NACALAI TESQUE, 04,404-26, 1:1000) and anti-PPP1r17 (Thermo Fisher, PA5-61599, 1:1000) were used. After washing with 0.01% Tween 20/PBS, the sections were stained with Alexa-conjugated secondary antibody (Thermo Fisher, 1:1000) in 1% BSA/0.3% Triton X-100/PBS with 10 μg/mL DAPI (NACALAI TESQUE, 11,034-56) for 1 h at room temperature. After washing with 0.01% Tween 20/PBS, the sections were mounted with ProLong Glass Antifade Mountant (Thermo Fisher) or Fluoromount (Diagnostic Biosystems).

For RNAscope analysis of the brain, the mice were anesthetized and perfused with 2% PFA/PBS. The isolated brain was postfixed overnight at 4°C, then transferred to 20% sucrose/PBS for cryoprotection, and embedded in OCT. The 15 μm-thick frozen sections were prepared by a cryostat. Air-dried sections were washed with PBS and baked for 30 min at 60°C. Then sections were fixed with 4% PFA/PBS for 15 min at 4°C. The slides were dehydrated with 50%, 70%, 100%, and 100% EtOH. The slides were treated with hydrogen peroxide solution to block endogenous HRP for 10 min at room temperature. After washing with distilled water, the sections were dehydrated with 100% EtOH for 5 min at room temperature. The sections were treated with Protease III for 30 min at 40°C

followed by washing with distilled water. The slides were then hybridized with an RNAscope probe for 2 h at 40°C. Mm-*Slc12a8* (846,551 and 846,731), Mm-*Slc17a6* (319,171), Mm-*Slc32a1* (319,191) and *Cre* (312,281) were used. The slides were washed with wash buffer. The RNAscope probe was hybridized with Multiplex FL v2 Amp 1, Multiplex FL v2 Amp 2, or Multiplex FL v2 Amp 3 for 30 min at 40°C. After washing, the signals were amplified with TSA Plus fluorophores. The slides were stained with DAPI in PBS, then mounted with ProLong Glass Antifade Mountant.

For immunohistochemical analysis of the longitudinal section of skeletal muscle, the TA muscles were isolated and fixed with 4% PFA/PBS for 30 min at 4°C, then transferred to 10% sucrose/PBS and 20% sucrose/PBS for cryoprotection, and embedded in OCT. The 30 μm-thick frozen sections were prepared by a cryostat. After air-dry, the sections were permeabilized and blocked with 5% goat serum/2% Triton X-100/PBS for 1 h at room temperature. The sections were then stained with first antibodies or reagents. Anti-TH (MERCK, AB152, 1:300), anti-neurofilament-H (Biolegend, 801,701, 1:1500) and Alexa 647 conjugated-α-BTX (Thermo Fisher, 1:500) in 5% goat serum/2% Triton X-100/PBS were used. After washing with 2% Triton X-100/PBS, the sections were stained with Alexa conjugated secondary antibodies in 1:1000 dilution for 1 h at room temperature. After washing and staining with DAPI, the sections were mounted with ProLong Glass Antifade Mountant.

For immunohistochemical analysis of the transverse section of skeletal muscle, isolated TA or GAS muscles were frozen in isopentane cooled by liquid nitrogen. The 8 μm-thick cryosections were cut across the middle part of the muscle. The air-dried sections were fixed with 4% PFA/PBS or cooled acetone for 10 min at room temperature. After washing with PBS, the sections were blocked with 5% goat serum/1% BSA/PBS for 15 min at room temperature. The sections were then stained with the first antibody or reagent. Anti β2AR (1:400), Alexa 555 conjugated-α-BTX (Thermo Fisher, 1:500), anti-type 1 fiber (Developmental Studies Hybridoma Bank, clone: BA-D5, 1:300), anti-type 2A fiber (Developmental Studies Hybridoma Bank, clone: SC-71, 1:200), anti-type 2B fiber (Developmental Studies Hybridoma Bank, clone: BF-F3, 1:400) or anti-laminin α2 (Enzo Life Sciences, clone: 4H8-2, 1:200) in 1% BSA/PBS were used. After washing with PBS, the sections were stained with Alexa conjugated secondary antibody in 1% BSA/PBS overnight at 4°C. After washing and staining with DAPI, the sections were mounted with Fluoromount. For NMJ analysis, the sections were observed using Leica fluorescence microscopy (Leica DM6 B). The average of TH signals around NMJs was quantified by ImageJ. Twelve-twenty nine NMJs in young mice and 23-42 NMJs in aged mice per mouse were analyzed. For the measurement of the cross-sectional area, the sections were observed using KEYENCE fluorescence microscopy. Approximately 40–150 type 1 fibers, 550-1020 type 2A fibers, and 920-3000 type 2B fibers were analyzed from one mouse.

For administration of tamoxifen, 100 mg/kg of tamoxifen in corn oil was administered to *Slc12a8-CreERT2* mice every day for 5 days followed by a 7-day recovery period.

Laser captured microdissection

Laser microdissection of hypothalamic subregions was performed as described previously with minor modifications (Johnson et al., 2018). Briefly, the brains from 3-4-months-old and 18-20-months-old mice were isolated and freshly frozen. The DMH, VMH, Arc, and LH were dissected by laser microdissection using the Leica LMD7000 (Leica Microsystems, USA). RNA from each hypothalamic subregion was isolated by PicoPure RNA Isolation Kit (Applied Biosystems). cDNA was generated from 16 ng of RNA with SuperScript IV VILO Master Mix (Invitrogen) and was used for qRT-PCR.

RNA isolation and reverse transcription-polymerase chain reaction analysis

RNA isolation and subsequent polymerase chain reaction (PCR) analysis were performed as described previously with minor modifications (Ito et al., 2018). Briefly, TA muscles were isolated at ZT15:00 and immediately frozen by liquid nitrogen. For the formoterol experiment, 0.2 mg/kg of formoterol was administered at ZT2:00, then TA muscles were isolated 6 or 12 h after administration. TRIzol (Invitrogen) was used for the isolation of total RNA. Single-strand cDNA was synthesized using a Superscript IV VILO Master Mix (Invitrogen). For quantitative reverse transcription (qRT)-PCR, the expression level of target genes was evaluated using TB Green Premix Ex Taq II on a QuantStudio 3 (applied biosystems). The primer sequences for qRT-PCR were as follow: *Slc12a8* forward 5′-ggcggtgtctactccatgat-3′, reverse 5′-agcacctgcaacacactgtc-3′, *PPARα* forward 5′-agaagttgcaggaggggatt-3′, reverse 5′-ttgaag gagctttgggaaga-3′, *PPARδ* forward 5′-gatggaagaccactcgcatt-3′, reverse 5′-aaccattgggtcagctcttg-3′, *PPARγ* forward 5′-gatggaa gaccactcgcatt-3′, reverse 5′-aaccattgggtcagctcttg-3′, *PDK4* forward 5′-tgactcaaagacgggaaacc-3′, reverse 5′-actggtcgcagag catcttt-3′, *Trim63* forward 5′-atggagaacctggagaagcagc-3′, reverse 5′-tggaagatgtcgttggcacac-3′, *Fbxo32* forward 5′-ccagcacacga caacacttcag-3′, reverse 5′-tatcccccgcagtttcaagc-3′. *TBP* forward 5′-cagcctcagtacagcaatcaac-3′, reverse 5′-taggggtcataggagt cattgg-3′. The expression level of each gene was normalized to that of *TBP*. For genotyping, KOD FX (TOYOBO, KFX-101, Japan) was used.

Western blotting

Western blotting was performed as described previously with minor modification (Ito et al., 2018). Briefly, TA muscles were isolated at ZT15:00. The isolated TA muscles were immediately frozen by liquid nitrogen. These muscles were dissected with a cryostat, and toral protein was extracted with a sample buffer containing 50 mM HEPES (pH 7.4), 4 mM EGTA, 10 mM EDTA, 15 mM $Na_4P_2O_7$, 25 mM NaF, 100 mM glycerophosphate, 5 mM Na_2VO_4, 0.1% Triton X-100 and a complete protease inhibitor cocktail (Roche, Basel, Switzerland). The concentration of extracted protein was determined by Coomassie Brilliant Blue G-250 (Bio-Rad, Hercules, CA, USA). Immediately before SDS-PAGE, the extracted protein solution was mixed with an equal volume of sample loading buffer

containing 30% glycerol, 62.5 mM Tris-HCl (pH 6.8), 2.3% SDS, 5% 2-mercaptoethanol, and 0.05% bromophenol blue. The mixed solution was heated at 60°C for 10 min. Thirty μg of extracted protein was separated on an SDS-polyacrylamide gel and transferred from the gel to a polyvinylidene difluoride membrane (Millipore, Burlington, MA, USA). The signals were detected by the ECL Western Blotting Detection system with Hyperfilm ECL. Anti-p-p70S6K (Thr389) (#9205, 1:400 for *in vivo* sample, 1:10,000 for *in vitro* sample), anti-p-p70S6K (Thr421/Ser424) (#9204, 1:2000 for *in vivo* sample, 1:120,000 for *in vitro* sample), anti-p70S6K (#2708, 1:100,000 for *in vivo* sample, 1:40,000 for *in vitro* sample), anti-p-S6 (Ser235/236) (#4858, 1:10,000 for *in vivo* sample, 1:100,000 for *in vitro* sample), anti-p-S6 (Ser240/244) (#5364, 1:40,000 for *in vivo* sample, 1:400,000 for *in vitro* sample), anti-S6 (#2217, 1:100,000), anti-p-Akt (Ser473) (#9271, 1:2000), anti-p-Akt (Thr308) (#13038, 1:20,000 for *in vivo* sample, 1:10,000 for *in vitro* sample), anti-Akt (#9272, 1:20,000), anti-p-FoxO1 (Ser256) (#9461, 1:1200), anti-FoxO1 (#2880, 1:4000), anti-p-FoxO3a (Ser253) (#13129, 1:800), anti-FoxO3a (#12829, 1:24,000) and anti-α-tubulin (#3873, 1:2000) were purchased from CST. Anti-p-PDH (Ser293) (NB110-93479, 1:4000) was purchased from NOVUS. Anti-PDHA1 (8D10 × 10^6, 1:12,000) and anti-β2AR (ab182136, 1:400,000) were purchased from Abcam. For rabbit polyclonal or monoclonal antibodies, HRP-conjugated anti-Rabbit IgG (GE, NA9340, 1:2000) was used for the secondary antibody. For mouse monoclonal antibodies, EasyBlot HRP-conjugated goat anti-mouse IgG antibody (GeneTex, GTX221667-01, 1:2000) was used for the secondary antibody.

For SUnSET analysis, 0.04 μmol/g body weight of puromycin was intraperitoneal administered. Thirty min after the administration, TA muscles were isolated and immediately frozen by liquid nitrogen. Puromycin-labeled peptides were detected by anti-puromycin antibody (Millipore, MABE343, 1:1000) and EasyBlot HRP-conjugated goat anti-mouse IgG secondary antibody (GeneTex, GTX221667-01, 1:2000). Coomassie Brilliant Blue staining was performed using CBB Stain One Super (NACALAI TESQUE).

Measurement of metabolites

TA muscles were isolated at ZT15:00 and immediately frozen by liquid nitrogen. These muscles were dissected by a cryostat. Intramuscular glycogen/glucose and pyruvate were analyzed using Glycogen Colorimetric/Fluorometric Assay Kit and Pyruvate Assay Kit (BioVision), respectively. For the measurement of pyruvate *in vitro*, primary myotubes were immediately frozen by liquid nitrogen. Intracellular pyruvate was extracted and analyzed by Pyruvate Assay Kit (BioVision).

The blood glucose level at ZT15:00 was analyzed by LAB Gluco (ForaCare Japan, Tokyo, Japan). For GTT, mice were fasted for 18 h, and 1.5 g/kg body weight of glucose was intraperitoneally administered. Plasma glucose levels at 15, 30, 60, and 120 min after the administration of glucose were measured by LAB Gluco. For ITT, mice were fasted for 18 h, and 0.6 mU/g body weight of insulin was intraperitoneally administered. Plasma glucose levels at 30, 60, 90, and 120 min after the administration of insulin were measured by LAB Gluco.

For the measurement of NAD/NADH, we used NAD/NADH-Glo Assay kit (Promega). After the infection of lentivirus, 2.0 x 10^4 cells were seeded onto 96-well plates. Twenty-four hours after passage, the cells were treated with 100 nM FK866 alone or FK866 with NMN. Twenty-four hours after the treatment, the cells were dissolved in NAD/NADH-Glo detection reagent and proceeded to the measurement of NAD/NADH.

QUANTIFICATION AND STATISTICAL ANALYSIS

All values are expressed as mean ± standard error of the mean (s.e.m.). The statistical significance of differences was assessed by Student's *t*-test for comparison of two groups, one-way analyses of variance (ANOVA) with Tukey's test for comparison of multiple groups, and two-way repeated-measures ANOVA for repeated measurement of two groups using Prism 8. Probabilities less than 5% (*, $p < 0.05$), 1% (**, $p < 0.01$) or 0.1% (***, $p < 0.001$), respectively, were considered to be statistically significant.

Cell Reports, Volume *40*

Supplemental information

Slc12a8 in the lateral hypothalamus maintains energy metabolism and skeletal muscle functions during aging

Naoki Ito, Ai Takatsu, Hiromi Ito, Yuka Koike, Kiyoshi Yoshioka, Yasutomi Kamei, and Shin-ichiro Imai

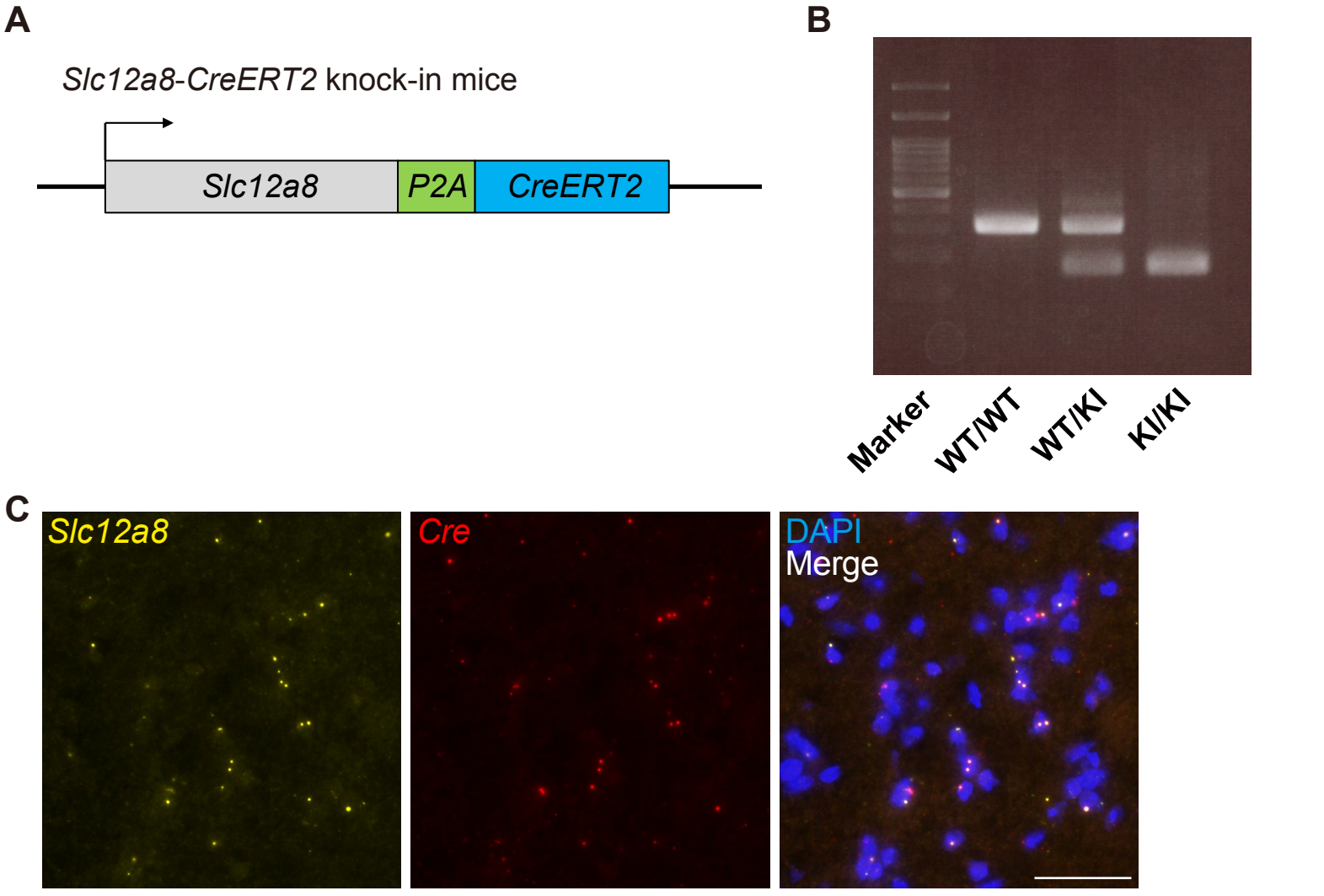

Figure S1. Related to Figure 1, Generation of *Slc12a8-CreERT2* mice.

(**A**) Schematic images for construction of *Slc12a8-CreERT2* mice. The *CreERT2* sequence was connected to the coding region of *Slc12a8* through the *P2A* sequence. (**B**) Representative image for genotyping of wild-type and *Slc12a8-CreERT2* mice. (**C**) Representative image for *Slc12a8* mRNA (yellow) and *Cre* (red) in the LH of *Slc12a8-CreERT2* mice by RNAscope. Bar: 50 μm. n=3.

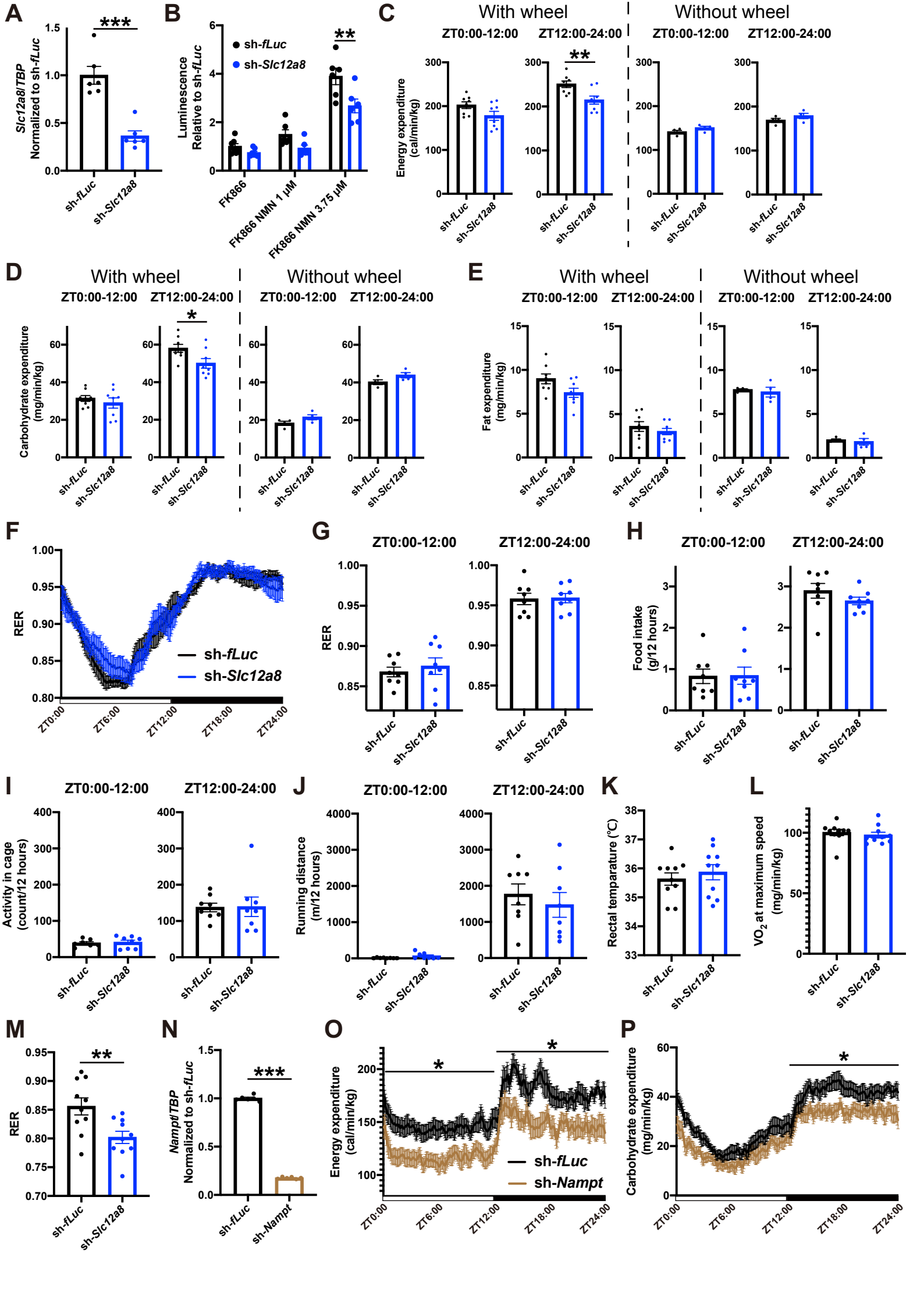
A
B
C
D
E
F
G
H
I
J
K
L
M
N
O
P
With wheel
Without wheel
ZT0:00-12:00
ZT12:00-24:00
sh-fLuc
sh-Slc12a8
sh-Nampt
FK866
FK866 NMN 1 μM
FK866 NMN 3.75 μM
Slc12a8/TBP Normalized to sh-fLuc
Luminescence Relative to sh-fLuc
Energy expenditure (cal/min/kg)
Carbohydrate expenditure (mg/min/kg)
Fat expenditure (mg/min/kg)
RER
Food intake (g/12 hours)
Activity in cage (count/12 hours)
Running distance (m/12 hours)
Rectal temparature (°C)
VO2 at maximum speed (mg/min/kg)
Nampt/TBP Normalized to sh-fLuc
ZT0:00
ZT6:00
ZT12:00
ZT18:00
ZT24:00

Figure S2. Related to Figure 2, *Slc12a8* in the lateral hypothalamus regulates energy expenditure and skeletal muscle functions.

(**A**) Knockdown efficiency for *Slc12a8* in Neuro2a cells. n=6. (**B**) NMN-induced increases in NAD^+ levels were analyzed in *Slc12a8*-knockdown Neuro2a cells. All cells were treated with 100 nM of FK866. n=6-7. (**C**-**E**) Average energy expenditure (**C**), carbohydrate expenditure (**D**) or fat expenditure (**E**) during ZT0:00-12:00 (left) or ZT12:00-24:00 (right) with or without running wheel in LH-specific *Slc12a8*-KD mice. n=4-8. (**F**) Metabolic cage analysis for RER of LH-specific *Slc12a8*-KD mice. n=8. (**G-J**) Average RER (**G**), food intake (**H**), open-field activity in a cage (**I**) or running distance by running wheel (**J**) during ZT0:00-12:00 (left) or ZT12:00-24:00 (right) in LH-specific *Slc12a8*-KD mice. n=8. (**K**) Rectal temperature of LH-specific *Slc12a8*-KD mice. n=10. (**L** and **M**) VO_2 (**L**) or RER (**M**) at maximum speed in LH-specific *Slc12a8*-KD mice. n=10. (**N**) Knockdown efficiency for *Nampt* in Neuro2a cells. n=6. (**O** and **P**) Metabolic cage analysis for energy expenditure (**O**) and carbohydrate expenditure (**P**) of LH-specific *Nampt*-KD mice. n=8. $*P < 0.05$, $**P < 0.01$ and $***P < 0.001$ by Student's *t*-test in (**A**), (**C**), (**D**), (**M**) and (**N**), by one-way ANOVA with Tukey's test in (**B**), or by two-way repeated-measures ANOVA in (**O**) and (**P**). Error bars indicate s.e.m.

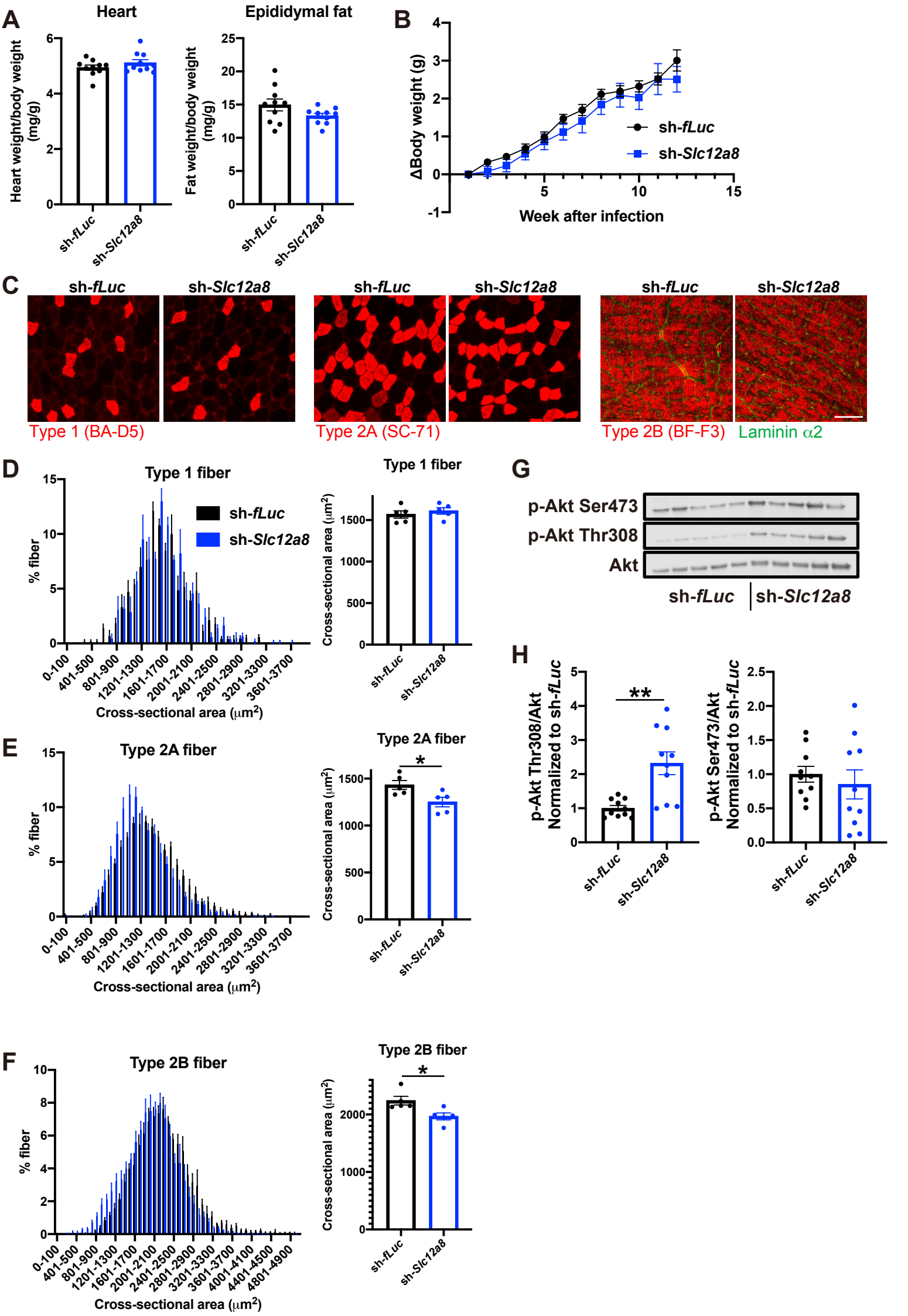
A
Heart
Heart weight/body weight (mg/g)
sh-fLuc
sh-Slc12a8
Epididymal fat
Fat weight/body weight (mg/g)
B
ΔBody weight (g)
sh-fLuc
sh-Slc12a8
Week after infection
C
sh-fLuc
sh-Slc12a8
Type 1 (BA-D5)
Type 2A (SC-71)
Type 2B (BF-F3)
Laminin α2
D
Type 1 fiber
% fiber
Cross-sectional area (μm²)
E
Type 2A fiber
F
Type 2B fiber
G
p-Akt Ser473
p-Akt Thr308
Akt
H
p-Akt Thr308/Akt Normalized to sh-fLuc
p-Akt Ser473/Akt Normalized to sh-fLuc

Figure S3. Related to Figure 3, *Slc12a8* in the lateral hypothalamus regulates muscle mass through protein synthesis.

(**A**) Heart weight (left) and epididymal fat weights (right) in LH-specific *Slc12a8*-KD mice. n=10. (**B**) Body weight changes in LH-specific *Slc12a8*-KD mice were comparable to those in control mice. n=15-35. (**C**) Representative image for Type 1 (left, red), Type 2A (middle, red) and Type 2B fibers (right, red). Type 2B fibers were co-stained with laminin α2 (right, green). Bar: 100 μm. (**D**-**F**) Left: The cross-sectional areas of type 1 fiber (**D**), type 2A fiber (**E**) or type 2B fiber (**F**). Right: The average cross-sectional areas of type 1 fiber (**D**), type 2A fiber (**E**) and type 2B fiber (**F**). n=5. (**G**) Representative Western blotting for phosphorylated and total Akt in TA muscles from LH-specific *Slc12a8*-KD mice. (**H**) Quantitative analysis for phosphorylation levels of Akt in LH-specific *Slc12a8*-KD mice. n=10. $*P < 0.05$ and $**P < 0.01$ by Student's *t*-test. Error bars indicate s.e.m.

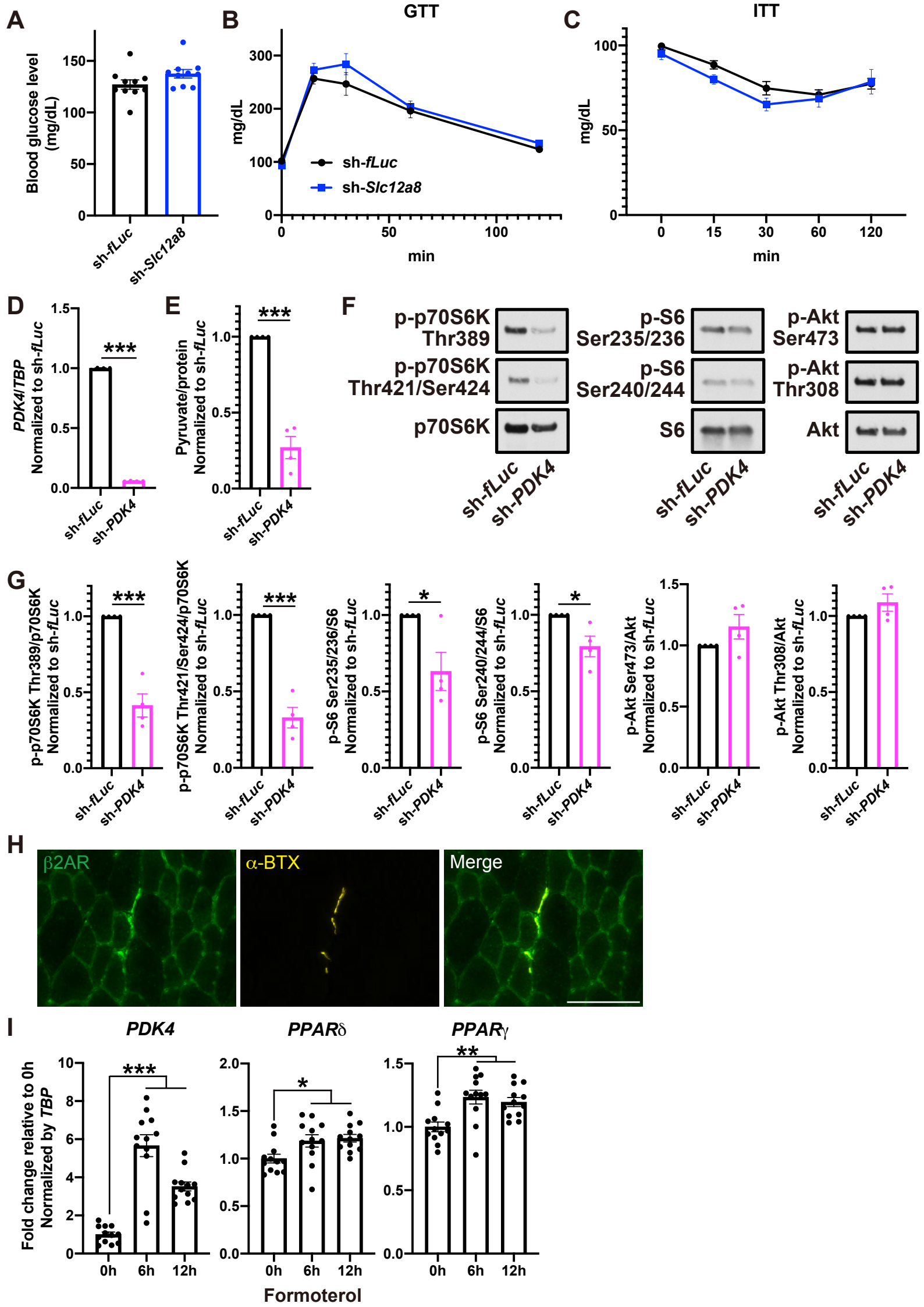
A
Blood glucose level (mg/dL)
150
100
50
0
sh-fLuc
sh-Slc12a8
B
GTT
mg/dL
300
200
100
0
sh-fLuc
sh-Slc12a8
0
50
100
min
C
ITT
mg/dL
100
50
0
0
15
30
60
120
min
D
PDK4/TBP
Normalized to sh-fLuc
1.5
1.0
0.5
0.0
***
sh-fLuc
sh-PDK4
E
Pyruvate/protein
Normalized to sh-fLuc
1.0
0.5
0.0
***
sh-fLuc
sh-PDK4
F
p-p70S6K Thr389
p-p70S6K Thr421/Ser424
p70S6K
p-S6 Ser235/236
p-S6 Ser240/244
S6
p-Akt Ser473
p-Akt Thr308
Akt
sh-fLuc
sh-PDK4
G
p-p70S6K Thr389/p70S6K
Normalized to sh-fLuc
p-p70S6K Thr421/Ser424/p70S6K
Normalized to sh-fLuc
p-S6 Ser235/236/S6
Normalized to sh-fLuc
p-S6 Ser240/244/S6
Normalized to sh-fLuc
p-Akt Ser473/Akt
Normalized to sh-fLuc
p-Akt Thr308/Akt
Normalized to sh-fLuc
1.5
1.0
0.5
0.0
***
*
sh-fLuc
sh-PDK4
H
β2AR
α-BTX
Merge
I
PDK4
PPARδ
PPARγ
Fold change relative to 0h
Normalized by TBP
10
8
6
4
2
0
2.0
1.5
1.0
0.5
0.0
***
*
**
0h
6h
12h
Formoterol

Figure S4. Related to Figure 4, *Slc12a8* in the lateral hypothalamus regulates glycolysis through the sympathetic nerve-β2AR axis.

(**A**) Fed blood glucose levels in LH-specific *Slc12a8*-KD mice was comparable to those in control mice. n=10. (**B**-**C**) No differences were observed in GTT (left) and ITT (right) in LH-specific *Slc12a8*-KD mice. n=9-10. (**D**) Knockdown efficiency for *PDK4* in primary myotubes. n=4. (**E**) Intracellular pyruvate levels in *PDK4*-knockdown primary myotubes. n=4. (**F**) Representative Western blotting for phosphorylated and total p70S6K, S6, and Akt in *PDK4*-knockdown primary myotubes. (**G**) Quantitative analysis of (**F**). n=4. (**H**) Representative images of β2AR and α-BTX (a maker of NMJ) in skeletal muscle. Bar: 100 μm. (**I**) The expression of *PDK4*, *PPAR*δ, and *PPAR*γ was induced by administration of formoterol. n=12. ***P < 0.001 by Student's *t*-test in (**D**), (**E**), and (**G**), or by one-way ANOVA with Tukey's test in (**I**). Error bars indicate s.e.m.

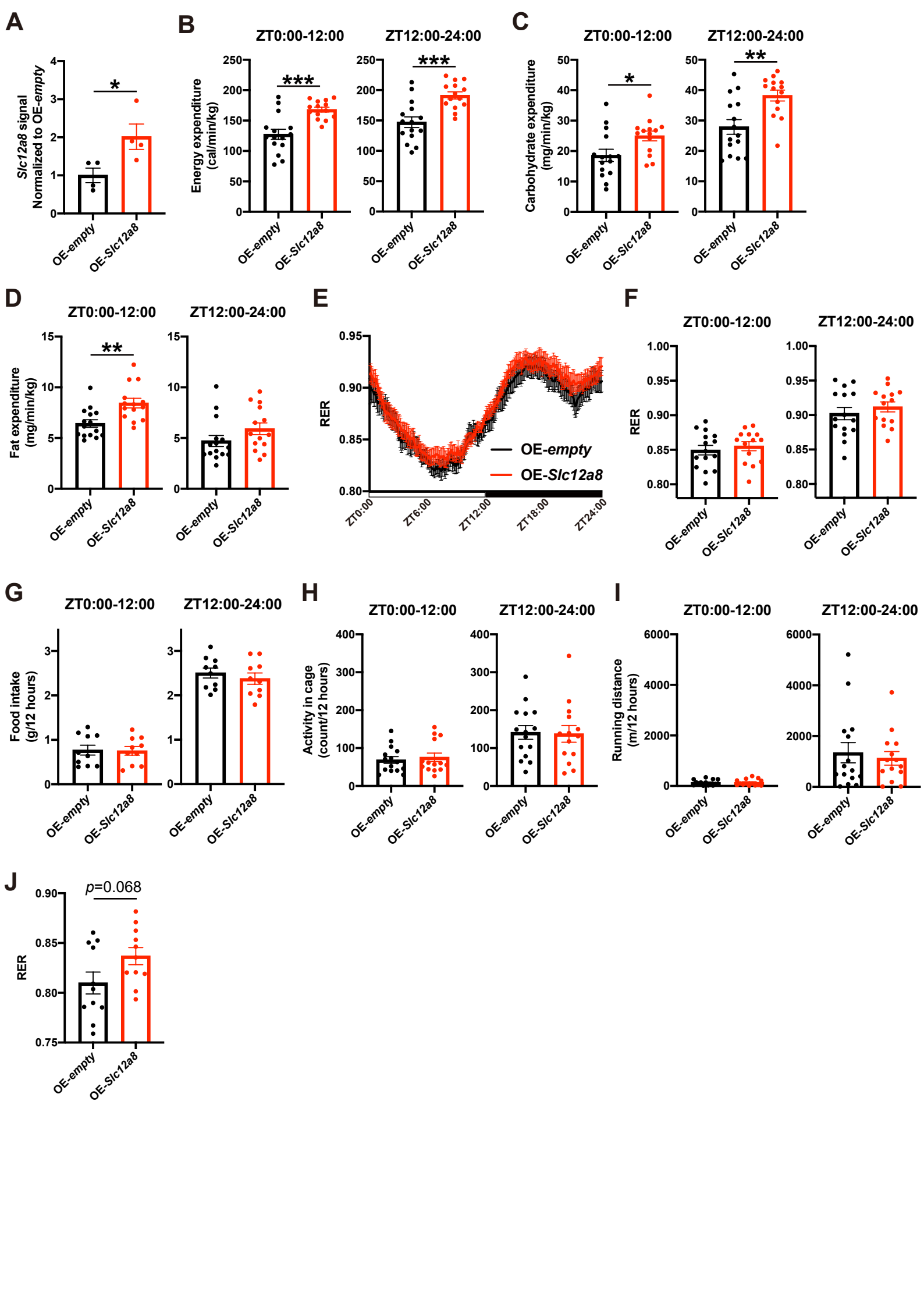
A
Slc12a8 signal Normalized to OE-empty
*
OE-empty
OE-Slc12a8
B
ZT0:00-12:00
ZT12:00-24:00
Energy expenditure (cal/min/kg)
***
***
C
ZT0:00-12:00
ZT12:00-24:00
Carbohydrate expenditure (mg/min/kg)
*
**
D
ZT0:00-12:00
ZT12:00-24:00
Fat expenditure (mg/min/kg)
**
E
RER
OE-empty
OE-Slc12a8
ZT0:00
ZT6:00
ZT12:00
ZT18:00
ZT24:00
F
ZT0:00-12:00
ZT12:00-24:00
RER
G
ZT0:00-12:00
ZT12:00-24:00
Food intake (g/12 hours)
H
ZT0:00-12:00
ZT12:00-24:00
Activity in cage (count/12 hours)
I
ZT0:00-12:00
ZT12:00-24:00
Running distance (m/12 hours)
J
p=0.068
RER

Figure S5. Related to Figure 6, Overexpression of *Slc12a8* in the lateral hypothalamus ameliorates age-associated decreases in energy expenditure, endurance capacity, and muscle force.

(**A**) Quantitative analysis for the overexpression of *Slc12a8* in the LH by RNAscope. n=4.

(**B-D**) Average energy expenditure (**B**), carbohydrate expenditure (**C**) or fat expenditure (**D**) during ZT0:00-12:00 (left) or ZT12:00-24:00 (right) in aged, LH-specific *Slc12a8*-OE mice. n=14-15.

(**E**) Metabolic cage analysis for RER in aged, LH-specific *Slc12a8*-OE mice. n=14-15. (**F-I**) Average RER (**F**), food intake (**G**), activity in cage (**H**) or running distance by running wheel (**I**) during ZT0:00-12:00 (left) or ZT12:00-24:00 (right) in aged, LH-specific *Slc12a8*-OE mice. n=14-15.

(**J**) RER at maximum speed in aged, LH-specific *Slc12a8*-OE mice. n=11. $*P < 0.05$, $**P < 0.01$ and $***P < 0.001$ by Student's *t*-test in (**A**), (**B**), (**C**), (**D**), and (**J**). Error bars indicate s.e.m.

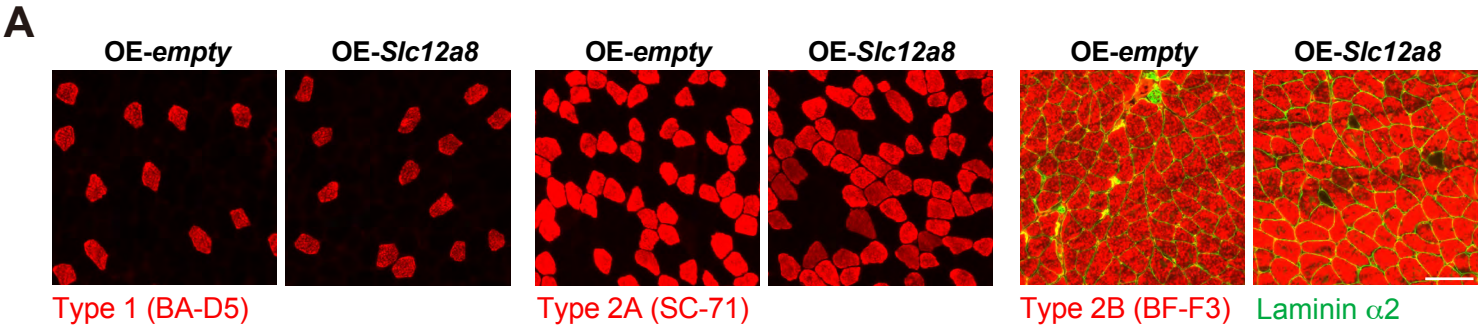
A
OE-empty
OE-Slc12a8
OE-empty
OE-Slc12a8
OE-empty
OE-Slc12a8
Type 1 (BA-D5)
Type 2A (SC-71)
Type 2B (BF-F3)
Laminin α2

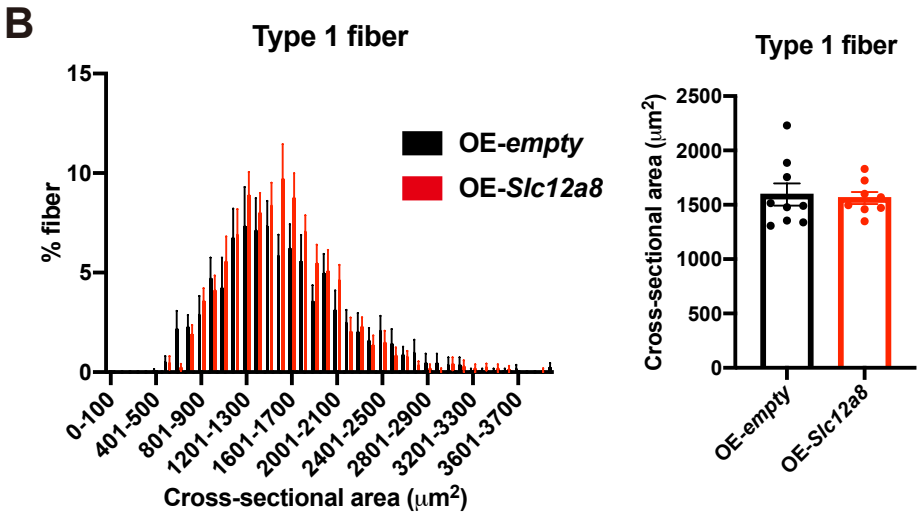
B
Type 1 fiber
% fiber
OE-empty
OE-Slc12a8
0-100
401-500
801-900
1201-1300
1601-1700
2001-2100
2401-2500
2801-2900
3201-3300
3601-3700
Cross-sectional area (μm²)

Type 1 fiber
Cross-sectional area (μm²)
OE-empty
OE-Slc12a8

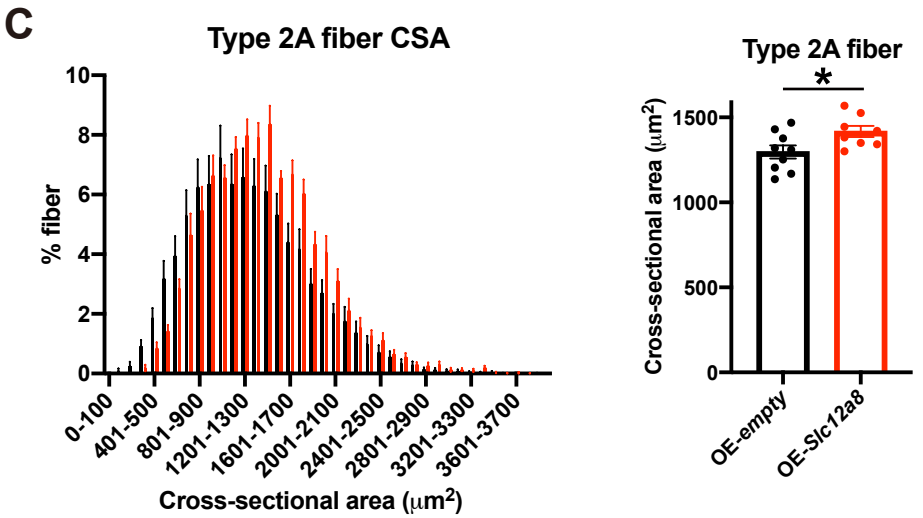
C
Type 2A fiber CSA
% fiber
0-100
401-500
801-900
1201-1300
1601-1700
2001-2100
2401-2500
2801-2900
3201-3300
3601-3700
Cross-sectional area (μm²)

Type 2A fiber
*
Cross-sectional area (μm²)
OE-empty
OE-Slc12a8

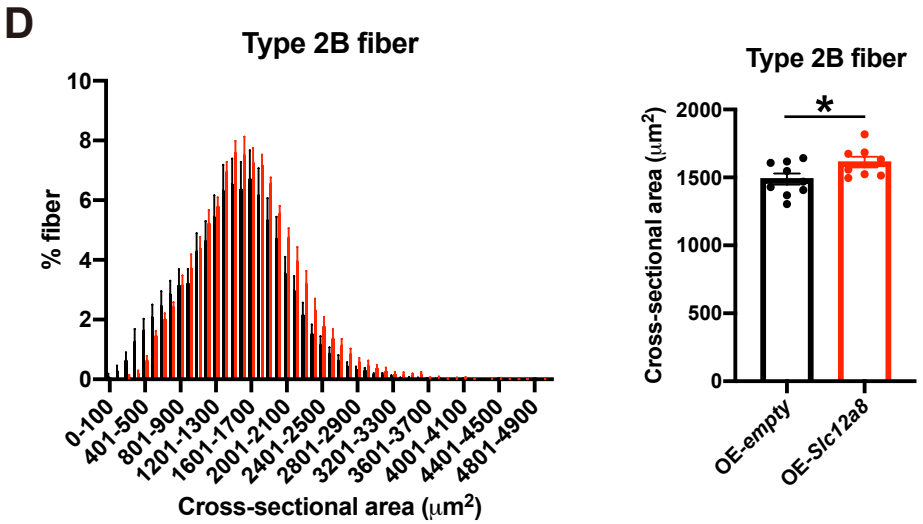
D
Type 2B fiber
% fiber
0-100
401-500
801-900
1201-1300
1601-1700
2001-2100
2401-2500
2801-2900
3201-3300
3601-3700
4001-4100
4401-4500
4801-4900
Cross-sectional area (μm²)

Type 2B fiber
*
Cross-sectional area (μm²)
OE-empty
OE-Slc12a8

Figure S6. Related to Figure 6, Overexpression of *Slc12a8* in the lateral hypothalamus ameliorates age-associated decreases in muscle cross-sectional area.

(**A**) Representative image for Type 1 (left, red), Type 2A (middle, red) and Type 2B fibers (right, red). Type 2B fibers were co-stained with laminin α2 (right, green). Bar: 100 μm.

(**B**-**D**) Left: The cross-sectional areas of type 1 fiber (**B**), type 2A fiber (**C**) or type 2B fiber (**D**). Right: The average cross-sectional areas of type 1 fiber (**B**), type 2A fiber (**C**) and type 2B fiber (**D**). n=8-9. **P* < 0.05 by Student's *t*-test. Error bars indicate s.e.m.